

Transient Turbulent Flow in a Liquid-Metal Model of Continuous Casting, Including Comparison of Six Different Methods

R. Chaudhary¹, C. Ji², B. G. Thomas¹, and S. P. Vanka¹

¹ Department of Mechanical Science & Engineering,
University of Illinois at Urbana-Champaign, Urbana, IL, USA

² School of Metallurgy & Ecology Engineering,
University of Science & Technology Beijing, China

Abstract

Computational modeling is an important tool to understand and stabilize transient turbulent fluid flow in the continuous casting of steel in order to minimize defects. The current work combines the predictions of two steady Reynolds-averaged Navier-Stokes (RANS) models, a “filtered” unsteady RANS model, and two large eddy simulation models with ultrasonic Doppler velocimetry (UDV) measurements in a small scale liquid GaInSn model of the continuous casting mold region fed by a bifurcated well-bottom nozzle with horizontal ports. Both mean and transient features of the turbulent flow are investigated.

LES outperformed all models while matching the measurements, except in locations where measurement problems are suspected. The LES model also captured high-frequency fluctuations, which the measurements could not detect. Steady RANS models were the least accurate methods. Turbulent velocity variation frequencies and energies decreased with distance from the nozzle port regions. Proper orthogonal decomposition analysis, instantaneous velocity patterns, and Reynolds stresses reveal that velocity fluctuations and flow structures associated with the alternating-direction swirl in the nozzle bottom, lead to a wobbling jet exiting the ports into the mold. These turbulent flow structures are responsible for patterns observed in both the time average flow and the statistics of their fluctuations.

Key words: LES, filtered URANS, RANS, turbulent flows, mold, SEN, continuous casting

I. INTRODUCTION

Optimization of fluid flow in the continuous casting process is important to minimize defects in steel products. Turbulent fluid flow in the submerged entry nozzle (SEN) and the mold are the main causes of entrainment of slag inclusions and the formation of surface defects [1]. Computational models combined with physical models are useful tools to study the complex turbulent flow in these systems [2].

Reynolds-averaged Navier-Stokes (RANS) models and water models are among the most popular techniques to analyze these systems [3-7]. Relatively few studies have exploited accurate fine-grid large eddy simulations (LES) to quantify transient flow in the nozzle and mold of continuous casting of steel [8-13] and even fewer have applied filtered unsteady RANS (URANS) models [14]. Yuan et al. [8] combined LES and particle image velocimetry (PIV) measurements in a 0.4 scale water model. The LES predictions matched well with the measurements. Transient oscillations were observed between two different flow patterns in the upper region: a wobbling stair-step downward jet, and a jet which bends midway between the narrow face and SEN. Long term flow asymmetries were observed in the lower region of the mold. Interaction of the flow from the two sides of the mold caused large velocity fluctuations near the top surface. Ramos-Banderas et al. [9] also found that LES model predictions agreed well with instantaneous velocity field measurements using digital PIV in a water model of a slab caster. Flow changed significantly due to vertical oscillations of the jet. Turbulence induced natural biasing without the influence of any other factors such as slide-gate, gas injection or SEN clogging. Instantaneous velocity showed periodic behavior and frequencies of this behavior were reported increasing with flow rate.

In another work, Yuan et al. [10] performed LES and inclusion transport studies in a water model and a thin slab caster. Complex time varying structures were found even in nominally steady conditions. The flow in the mold switched between double-roll flow and complex flow with many rolls. Zhao et al. [11] performed LES with superheat transport and matched model predictions with plant and full scale water model measurements. The jet exiting the nozzle showed chaotic variations with temperature fluctuations in the upper liquid pool varying $\pm 4^{\circ}\text{C}$ and heat flux $\pm 350 \text{ kW/m}^2$. Addition of the static-k SGS model had only minor effects.

Qian et al [12] employed LES with a DC magnetic field effects in a slab continuous casting process. A new vortex brake was proposed and its effect on vortex suppression was studied. The effect of the location of the magnetic field brake on vortex formation was also studied. The magnetic brake, when applied at free surface, suppressed turbulence and biased vortices significantly. Liu et al. [13] applied LES in a continuous casting mold to study the transient flow patterns in the upper region. The turbulent asymmetry in the upper region was reported all the times. The upper transient roll was found to break into number of small scale vortices.

Very few previous studies have been undertaken to evaluate the accuracy of turbulent flow simulations with measurements. One of the few [15] found that flow simulations using both LES with the classical Smagorinsky sub-grid scale model, and RANS with the standard k- ϵ model, showed good quantitative agreement with time-average velocity measurements in a 0.4 scale water model using PIV, and in an operating slab casting machine using an electromagnetic probe. Another [16] showed that very fine meshes were required, and that imposing symmetry could drastically change the LES flow pattern.

This work investigates transient turbulent flow in the nozzle and mold of a typical continuous casting process by comparing computations with previous horizontal velocity measurements [17-19] using ultrasonic Doppler velocimetry (UDV) in a GaInSn model of the process. In addition, it evaluates the accuracy and performance of five different computational models, including two LES models, a “filtered” URANS model, and two steady RANS models for such flows. In addition, Reynolds stresses, turbulent kinetic energy (TKE), and power spectra are presented and analyzed. The LES instantaneous velocities were further processed to perform proper orthogonal decomposition (POD) to identify significant modes in the turbulent velocity fluctuations.

II. VELOCITY MEASUREMENTS USING ULTRASONIC DOPPLER VELOCIMETRY

Velocity measurements were performed in a GaInSn model of the continuous casting process at Forschungszentrum Dresden-Rossendorf (FZD), Dresden, Germany [17-19]. Figure 1(a), 1(b) and 2(c) respectively show the front, side and bottom views of the model. The GaInSn eutectic metal alloy is liquid at room temperature (melting point $\sim 10^\circ\text{C}$). Liquid GaInSn from the tundish flows down a 10-mm diameter 300-mm long SEN, exiting through two horizontal (zero degree

angle) nozzle ports into a Plexiglas mold with 140mm (width) x 35mm (thickness) and vertical length of ~300mm. The bifurcated nozzle ports were rectangular 18mm high X 8mm wide, with 4-mm radius chamfered corners. The liquid metal free surface level was maintained around 5 mm below mold top. The liquid metal flows out of the mold bottom from two 20-mm diameter side outlet pipes.

Ultrasonic Doppler Velocimetry (UDV) was used to measure horizontal velocity in the mold midplane between wide faces by placing 10 ultrasonic transducers along the narrow face spaced 10 mm apart vertically and facing towards SEN. Each transducer measured instantaneous horizontal velocity along a horizontal line comprising the axis of the ultrasound beam. The velocity histories were collected along the 10 lines for around 25 sec to create 125 frames. These measurements were performed using a DOP2000 model 2125 velocimeter (Signal Processing SA, Lausanne) with ten 4-MHz transducers (TR0405LS, active acoustic diameter 5 mm). More details on these measurements can be found in [17-19].

III. COMPUTATIONAL MODELS

1. *Standard k-ε Model (SKE)*

In steady-state Reynolds-averaged Navier-Stokes (RANS) methods, the ensemble-averaged mass (continuity) and momentum balance equations are given as [20-21]:

$$\frac{\partial \bar{u}_i}{\partial x_i} = 0 \quad (1)$$

$$\frac{\partial \bar{u}_i}{\partial t} + \frac{\partial \bar{u}_i \bar{u}_j}{\partial x_j} = -\frac{1}{\rho} \frac{\partial \bar{p}^*}{\partial x_i} + \frac{\partial}{\partial x_j} \left((\nu + \nu_t) \left(\frac{\partial \bar{u}_i}{\partial x_j} + \frac{\partial \bar{u}_j}{\partial x_i} \right) \right) \quad (2)$$

Where, the modified pressure is $\bar{p}^* = \bar{p} + \frac{2}{3} \rho k$. The above equations are solved after dropping the first term and using turbulent (eddy) viscosity,

$$\nu_t = C_\mu k^2 / \varepsilon \quad (3)$$

where the model constant $C_\mu = 0.09$. This approach requires solving two additional scalar transport equations for the k and ε fields. The standard $k-\varepsilon$ model is widely used in previous work, and further details can be found in [22], [23] and [24]. The enhanced wall treatment (EWT) [23, 25-26] is used for wall boundaries and the equations are solved using FLUENT [24].

2. *Realizable k- ε model (RKE)*

The Realizable $k-\varepsilon$ model [27] is another steady RANS model similar to the standard $k-\varepsilon$ model. This model ensures that Reynolds normal stresses are positive and satisfies the Schwarz inequality ($\overline{u'_i u'_j}^2 \leq \overline{u'^2_i} \overline{u'^2_j}$), which may be important in highly strained flows. These “realizable” conditions are achieved by making C_μ a special function of the velocity gradients and k and ε . In addition to C_μ , the RKE model also has some different terms in the dissipation rate (ε) transport equation, which is derived from the exact transport equation of mean-square vorticity fluctuations, $\varepsilon = \nu \overline{\omega_i \omega_i}$, where vorticity, $\omega_i = \frac{\partial u'_k}{\partial x_j} - \frac{\partial u'_j}{\partial x_k}$. More details on the formulations of RKE are given in [27, 23-24].

3. *“Filtered” Unsteady RANS Model (URANS)*

Unsteady RANS (URANS) models solve the transient Navier Stokes Eqs. 1-2. Results with standard $k-\varepsilon$ URANS always exhibit excessive diffusion, and in some flows, almost match steady-RANS, showing almost no time variations [28]. In the “filtered” URANS approach, the eddy viscosity is decreased to lessen this problem of excessive diffusion, while capturing the large-scale transient features of turbulent flows. Johansen et al [28] improved on the standard $k-\varepsilon$ model by redefining the turbulent viscosity as:

$$\nu_t = C_\mu \min(1.0, f) k^2 / \varepsilon \quad (4)$$

where, $f = \Delta \varepsilon / k^{3/2}$, and Δ is the constant filter size defined as the cube root of the maximum cell volume in the domain or 2.16mm here. For fine grids, f is smaller than 1, so ν_t decreases, and there is less “filtering” of the velocities relative to the standard SKE URANS. This turbulent

viscosity model was implemented in the current work into the standard k- ϵ model in FLUENT via a user defined function (UDF) and solved with EWT at wall boundaries.

4. Large Eddy Simulations with CU-FLOW [29-31]

The 3-D time dependent filtered Navier-Stokes (N-S) equations and continuity equation for large eddy simulations can be written as [20-21],

$$\frac{\partial u_i}{\partial x_i} = 0 \quad (5)$$

$$\frac{\partial u_i}{\partial t} + \frac{\partial u_i u_j}{\partial x_j} = -\frac{1}{\rho} \frac{\partial p^*}{\partial x_i} + \frac{\partial}{\partial x_j} \left((\nu + \nu_s) \left(\frac{\partial u_i}{\partial x_j} + \frac{\partial u_j}{\partial x_i} \right) \right) \quad (6)$$

Where, the modified pressure is $p^* = p + \frac{2}{3} \rho k_r$, k_r is residual kinetic energy.

The “sub-grid scale” (SGS) viscosity, ν_s , [21] needed to “close” this system can be found using any of several different models, including the classical Smagorinsky model [32], dynamic Smagorinsky-Lilly model [33-35], dynamic kinetic energy sub-grid scale model [36] and the wall-adapting local eddy-viscosity (WALE) model [37]. Among these popular models, the WALE model is mathematically more reasonable and accurate in flows involving complicated geometries [37]. This model captures the expected variation of eddy viscosity with the cube of distance close to the wall without any expensive or complicated dynamic procedure or need of Van-driest damping as a function of y^+ , which is difficult in a complex geometry [37]. The WALE SGS model is used in the current work and is defined as [37],

$$\nu_s = L_s^2 \frac{(S_{ij}^d S_{ij}^d)^{3/2}}{(S_{ij} S_{ij})^{5/2} + (S_{ij}^d S_{ij}^d)^{5/4}} \quad (7)$$

where, $S_{ij} = \frac{1}{2} \left(\frac{\partial u_i}{\partial x_j} + \frac{\partial u_j}{\partial x_i} \right)$,

$$S_{ij}^d = \frac{1}{2} (g_{ij}^2 + g_{ji}^2) - \frac{1}{3} \delta_{ij} g_{kk}^2, \quad g_{ij}^2 = g_{ik} g_{kj}, \quad g_{ij} = \frac{\partial u_i}{\partial x_j}, \quad \delta_{ij} = 1, \text{ if } i=j, \text{ else } \delta_{ij} = 0$$

and $\Delta = (\Delta x \Delta y \Delta z)^{1/3}$, Δx , Δy , and Δz are the grid spacing in x, y and z directions.

For the CU-FLOW LES model, the length scale is defined as $L_s = C_w \Delta$, $C_w^2 = 10.6 C_s^2$ [37] and C_s is Smagorinsky constant taken to be 0.18 [37]. The advantage of this method is that the SGS model viscosity converges towards the fluid kinematic viscosity ν as the grid becomes finer and Δ becomes small.

Near-Wall Treatment

A wall-function approach given by Werner-Wengle [38] is used for the LES models, to compensate for the relatively coarse mesh necessarily used in the nozzle and the highly turbulent flow ($Re \sim 41,000$, based upon nozzle bore diameter and bulk axial velocity). This wall treatment assumes a linear profile ($U^+ = Y^+$ for $Y^+ = y u_\tau / \nu \leq 11.8$) combined with a power law profile ($U^+ = A(Y^+)^B$ for $Y^+ > 11.8$) for the instantaneous tangential velocity in each cell next to a wall boundary, assuming $A = 8.3$, $B = 1/7$. These velocity profiles are analytically integrated in the direction normal to the wall to find the cell-filtered tangential velocity component u_p in the cell next to the wall, which is then related to instantaneous filtered wall shear stress [38].

When $|u_p| \leq \mu / (2\rho\Delta z) A^{2/(1-B)}$, i.e. the cell next to the wall is in viscous sublayer, the wall stress in the tangential momentum equations is imposed according to a standard no slip wall boundary condition,

$$|\tau_w| = 2\mu |u_p| / \Delta z \quad (8)$$

where Δz is the thickness of the near-wall cell in the wall normal direction.

Otherwise, when $|u_p| > \mu / (2\rho\Delta z) A^{2/(1-B)}$, the wall stress in Eq. (8) is replaced by the following wall stress defined by Werner-Wengle [38]:

$$|\tau_w| = \rho \left[(1-B) / 2 A^{\frac{1+B}{1-B}} (\mu / (\rho\Delta z))^{1+B} + \frac{1+B}{A} (\mu / (\rho\Delta z))^B |u_p| \right]^{\frac{2}{1+B}} \quad (9)$$

In both situations, the wall is impenetrable and wall normal velocity is zero.

5. LES FLUENT

The commercial code, FLUENT [24], was also used to solve the same equations given in Section III-4, with the exception that L_s and C_s were instead defined as:

$$L_s = \min(\kappa d, C_w \Delta), \quad C_w^2 = 10.6 C_s^2, \quad \kappa = 0.418 \quad \text{and} \quad C_s = 0.10 \quad (10)$$

where, d is distance from cell center to the closest wall. The lower value of $C_s = 0.10$ has been claimed to sustain turbulence better on relatively coarse meshes [37, 39, 24].

IV. MODELLING DETAILS

The five different computational models were applied to simulate fluid flow in the GaInSn model described in Section III. The computational domains are faithful reproductions of the nozzle and mold geometries shown in Figure 1, except near the outlet. Realizing the only small importance of the bottom region and the difficulty in creating hexahedral meshes, the circular bottom outlets are approximated with equal-area rectangular outlets. This approximation also changes the shape of the mold bottom, as shown in Figure 1(c) and (d). Further details on the dimensions, process parameters (Casting speed, flow rate etc.) and fluid properties (density and viscosity) [17-19] are presented in Table 1.

A. DOMAINS AND MESHES

To minimize computational cost, the two-fold symmetry of the domain was exploited for the RANS (RKE and SKE) simulations. Specifically, one quarter of the combined nozzle and mesh

domain was meshed using a mostly-structured mesh of ~0.61 million hexahedral cells. Figure 2(a) and 2(b) respectively show an isometric view of the mesh of the mold and port region used in the steady RANS calculations.

In the “filtered” URANS and LES calculations, time dependent calculations of turbulent flow required simulation of the full 3-D domain. The combined nozzle and mold meshes used in the URANS and LES-FLUENT simulations had similar cells as the steady RANS models, but with a total of ~0.95 million and ~1.33 million hexahedral cells respectively. The LES-CU-FLOW simulation used a much finer mesh (~5 times bigger than LES-FLUENT) with ~7 million (384x192x96) brick cells. Figure 2(c) and 2(d) respectively show the brick mesh used in LES-CU-FLOW near the nozzle port and mold mid-plane.

B. BOUNDARY CONDITIONS

In the steady RANS and “filtered” URANS models, a constant velocity condition was used at the nozzle inlet ($U_m = 1.4$ m/s, equivalent to 110ml/sec flow rate) with k and ε values of $0.01964\text{m}^2/\text{s}^2$ and $0.55\text{m}^2/\text{s}^3$ respectively calculated using relations ($k = 0.01U_m^2$, and $\varepsilon = k^{1.5} / 0.05D$, where D is hydraulic diameter) given by [40]. The LES-FLUENT model used the same nozzle length and constant velocity profile, fixed at the mean velocity without any perturbation. Flow in this straight pipe extending down from the tundish bottom was able to develop accurate fully-developed turbulence, owing to the long $L/D=30$.

In LES-CU-FLOW, the nozzle bore was truncated at the level of the liquid surface in the mold to lessen the computational burden. This gives L/D of ~7.2 which is not sufficient for flow to develop in the nozzle. Due to this shorter bore length, an inlet mapping condition proposed in [41] was implemented to make the flow develop within the short distance. In this condition, all three velocity components at the inlet were copied from a downstream section at $L/D=4$ with the axial velocity component multiplied by a factor of $Q_{\text{required}} / Q_{\text{at } L/D=4}$ in order to maintain the desired flow rate (Q_{required}) against frictional losses.

In both LES and RANS, the top surface of the mold was taken to be a free-slip boundary. All solid domain walls were given no-slip conditions using EWT in RANS (RKE and SKE) models, and the Werner-Wengle formulation in LES. In LES-FLUENT, the outlets at the mold bottom were given a constant pressure “outlet” boundary condition (0 Pa gauge). In LES-CU-FLOW, the domain outlets were truncated even with the narrow face walls and the following convective outlet boundary condition was implemented in implicit form for all three velocity components [42],

$$\partial \vec{V} / \partial t + U_{\text{convective}} \partial \vec{V} / \partial n = 0, \text{ where } \vec{V} = u, v, w \quad (11)$$

Where $U_{\text{convective}}$ is set to the average normal velocity at the outlet plane. To maintain the required flow rate, the outlet normal velocity from Eq. (11) is corrected between iterations as follows:

$$u_{\text{normal}}^{\text{new}} = (Q_{\text{required}} - Q_{\text{current}}) / \text{Area}_{\text{outlet}} + u_{\text{normal}} \quad (12)$$

C. NUMERICAL METHODS

During steady RANS calculations, the ensemble-averaged equations for the three momentum components, turbulent kinetic energy (k-), dissipation rate (ϵ -), and Pressure Poisson Equation (PPE) are discretized using the Finite Volume Method (FVM) in FLUENT [24] with either 1st or 2nd-order upwind schemes for convection terms. Both upwind schemes were investigated to assess their accuracy. These discretized equations are then solved using the segregated solver for velocity and pressure using the semi-implicit pressure linked equations (SIMPLE) algorithm, starting with initial conditions of zero velocity in the whole domain. Convergence was defined when the unscaled absolute residuals in all equations reduced below 1×10^{-04} .

In “filtered” URANS calculations, the same ensemble averaged equations as in steady SKE RANS with EWT were solved at each time step using the segregated solver in FLUENT after implementing the filtered eddy viscosity using a UDF. Convection terms were discretized using 2nd order upwind scheme. The implicit fractional step method was used for pressure-velocity coupling with the 2nd order implicit scheme for time integration. For convergence, the scaled residuals were reduced by 3 orders of magnitude every timestep ($\Delta t = 0.004$ sec). Starting from

initial conditions of zero velocity in the whole domain, turbulent flow was allowed to develop by integrating the equations for 20.14 sec before collecting statistics. After reaching stationary turbulent flow in this manner, velocities and turbulence statistics were then collected for ~ 31 sec. URANS solves two additional transport equations for turbulence k and ϵ , so is slower than LES for the same mesh per timestep. Adopting a coarser mesh, which allows a larger timestep, makes this method much more economical than LES overall. More on this will be discussed in the following computational cost section.

In LES-CU-FLOW, the filtered LES equations Eqs. (5-7) were discretized using the FVM on a structured Cartesian staggered grid. Pressure-velocity coupling is resolved through a fractional step method with explicit formulation of the diffusion and convection terms in the momentum equations with the Pressure Poisson Equation (PPE). Convection and diffusion terms were discretized using the second order central differencing scheme in space. Time integration used the explicit second order Adams-Bashforth scheme. Neumann boundary conditions are used at the walls for the pressure fluctuations (p'). The PPE equation was solved with a geometric multigrid solver. The detailed steps of this method are outlined in Chaudhary et al. [29]. Every time step, residuals of PPE are reduced by 3 orders of magnitude. Starting with a zero velocity field, the flow-field was allowed to develop for ~ 21 sec and then mean velocities were collected for ~ 3 sec (50,000 timesteps, $\Delta t = 0.0006$ sec). Finally, mean velocities, Reynolds stresses and instantaneous velocities were collected for a further 25.14 sec.

In LES-FLUENT, the filtered equations were discretized and solved in FLUENT using the same methods as the “filtered”-URANS model, except for using a much smaller timestep ($\Delta t = 0.0002$ sec), and basing convergence on the unscaled residuals. Flow was allowed to develop for 23.56 sec before collecting results for a further 21.48 sec.

D. COMPUTATIONAL COST

The computations with FLUENT (RANS, URANS and LES) were performed on an 8-core PC with a 2.66 GHz Intel[®] Xeon processor (Intel Corp., Santa Clara, US) and 8.0 GB RAM, using 6 cores for steady RANS and LES and 3 cores for “filtered” URANS. The quarter-domain steady RANS models (RKE and SKE) took ~ 8 hrs CPU time total. The full-domain “filtered” URANS

model took ~ 28 sec per timestep, or ~ 100 hrs total CPU time for the 51 sec simulation. Thus, the steady RANS models are over one order of magnitude faster than URANS to compute the time-average flow pattern.

The full-domain LES-FLUENT model took ~ 26 sec per timestep or ~ 1626 hours (67 days) total CPU time for the total 225,200 timesteps of the total 45 sec simulation (23.5s flow developing + 21.5 (averaging time)). Considering the similar mesh sizes, the filtered URANS model (0.95 million cells) is more than one order of magnitude faster than the LES model (1.33 million cells) using FLUENT. The steady RANS models are over 200 times faster than this LES model, because they can exploit a coarser mesh and finish in one step.

LES calculations using CU-FLOW were performed on the same computer but using the installed graphic processing unit (GPU). CU-FLOW took around 13 days to simulate ~ 48 sec. Thus, LES-CU-FLOW is about five times faster than LES-FLUENT. Considering its five-times better-refined mesh, (~ 7 million cells) and the 6 processing cores used by FLUENT, CU-FLOW is really more than two orders of magnitude faster than LES-FLUENT. This shows the great advantage of using better algorithms, which also can exploit the GPU.

V. COMPARISON OF COMPUTATIONS AND MEASUREMENTS

The predictions of the five different computational models first validated with pipe flow measurements, and then are compared with the UDV measurements in the mold apparatus. Further comparisons between models and measurements in this apparatus are given throughout the rest of this paper, including comparisons of time-averaged velocities in the nozzle and mold, averaged turbulence quantities, and instantaneous velocity traces at individual points.

Nozzle Bore

Flow through the nozzle controls flow in the mold, so the time/ensemble average axial velocity in the SEN bore is presented in Figure 3 comparing the model predictions, with measurements by Zagarola et al [43] of fully-developed pipe flow at a similar Reynolds number ($Re_D = DU/v \sim 42,000$). All models match the measurements [43] closely, except for minor differences in the core and close to the wall. The RANS methods match well here because this is a wall-attached

flow at high Reynolds number, and these models were developed for such flows. The results from URANS are quite similar to steady SKE RANS so are not presented. Velocity from LES-CU-FLOW also matches very closely at both distances down the nozzle ($L/D=3$ and 6.5 below the inlet), which validates the mapping method described in Section IV-B to achieve fully-developed, transient turbulent flow within a short distance. The minor differences are due to the coarse mesh for this high Reynolds number preventing LES from completely resolving the smallest scales close to the wall. Overall, the reasonable agreement in the nozzle bore of all models with this measurement demonstrates an accurate inlet condition for the mold predictions.

Mold

All five models are next compared with the UDV measurements in the liquid-metal-filled mold. Figure 4 compares the time/ensemble average horizontal velocity at the mold midplane as contour plots. Figure 5 compares these horizontal velocity predictions along three horizontal lines (95 mm, 105mm 115 mm from mold top) at the mold mid-plane between wide faces. The time-averaging range for the three transient models were 31.19s (SKE URANS), 21.48s (LES-FLUENT), and 25.14s (LES-CU-FLOW) which can be compared with 24.87s of time averaging of the measured flow velocities.

LES is seen to match best with the measurements. Due to the small number of data frames in the measurements (~ 125 over 24.87 sec), the time averages show some wiggles. Close to the SEN and narrow-face walls, the measurements give inaccurate zero values, perhaps due to distance from the sensor and/or interference from the walls of the nozzle and narrow face. Its match with measurements along the 3 lines in Figure 5 is almost perfect. Furthermore, it matched well with the low values measured along seven other lines (not presented). Based on this agreement and its physically reasonable predictions near walls, the LES predictions are concluded to be more accurate than the measurements, at least for the evaluation of the other models.

Minor differences between CU-FLOW and FLUENT LES predictions are seen. The CU-FLOW velocities show a wider spread of the jet with a stronger “nose” at port outlet, compared to FLUENT. This effect is more realistic and physically expected due to the transient stair-stepping

behavior of the swirling jet exiting the nozzle port. It shows that the flow pattern is more accurately resolved by CU-FLOW, owing to its much finer mesh (~ 5.3 times).

The other models show less accurate predictions than LES in both jet shape (Figure 4) and horizontal velocity profiles (Figure 5). The jet from steady SKE is thinner and directed straighter towards the narrow face, due to the inability of this steady model to capture the real transient jet wobbling. More jet spreading is predicted with 1st-order upwinding than with the second-order scheme of the steady SKE model. This is caused by the extra numerical diffusion of the 1st order scheme, which makes it match closer with both the measurements and the LES flow pattern. When considering its better numerical stability and simplicity, the 1st-order scheme is better than the higher order scheme for this problem. Among the steady RANS models (SKE and RKE), SKE matched more closely, so was selected for URANS modeling and further steady-RANS evaluations. The “filtered” URANS model resolves turbulence scales bigger than the filter size and smaller scales are modeled with the two-equation k - ϵ model. This model captures some jet wobbling and thus gives predictions somewhat in between LES and steady RANS. Overall, all methods agreed reasonably well, with the RANS models being least accurate, URANS next, followed by measurements, LES-FLUENT, and LES-CU-FLOW being most accurate.

VI. TIME-AVERAGED RESULTS

A. Nozzle flow

In addition to the line-plot comparison of axial velocity in the nozzle bore with measurements (Figure 3), model predictions of axial velocity contours and secondary velocity vectors are compared in Figure 6. The SKE, filtered URANS and LES-FLUENT models exhibit almost no secondary flows (Figure 6(a)). Interestingly, the stair-step mesh in CU-FLOW generates minor mean secondary flows which have a maximum magnitude of around $\sim 2\%$ of the mean axial velocity through the cross-section (Figure 6(b)). These secondary flows move towards the walls from the core in four symmetrical regions. This causes slight bulging of the axial velocity which is similar to secondary flow in a square duct at the corners bisectors [29]. These very small secondary flows have negligible effects on flow in the nozzle bottom and mold.

The jets leaving the nozzle ports directly control flow in the mold, so a more detailed evaluation of velocity in the nozzle bottom region was performed. The predicted velocity magnitude contours at the nozzle bottom mid-plane are compared in Figure 7(a)-(d). Qualitatively, the flow patterns match reasonably well in all models, except for minor differences in the steady SKE model. This reasonable match by steady SKE, comparable with other transient methods, is expected due to the high Reynolds number flow ($Re \sim 42,000$) in the entire nozzle, for which steady SKE model is most suitable. Flow patterns with LES-CU-FLOW and LES-FLUENT are very similar.

The jet characteristics [44] exiting the nozzle port predicted by different models are summarized in Table 2. Significant differences are seen between the different models. The steady SKE gives a bigger back flow region (34%), and URANS a smaller one (17.6%), compared to LES-FLUENT (25.1%). Although the weighted downward velocity is quite similar (within $\sim 8\%$) in all models, the weighted outward and horizontal velocities are quite different. Thus, the jet angles differ significantly, which greatly affects mold flow. The steady SKE model predicts the shallowest downward jet angle, and the “filtered” URANS model the steepest. The URANS model also predicts the largest horizontal spread angle (9.2 degree).

A comparison of velocity magnitude along the mid-port- and 2-mm-forward-offset vertical lines is presented in Figure 8. In the upper back flow region, all models agree, but significant differences are seen in the lower outward flow region. In the outward flow region, a high velocity convex profile is predicted along the midport, while a lower-velocity with a humped profile is seen along the offset line. This hump is due to swirling flow inside the nozzle. Although LES-CU-FLOW and LES-FLUENT velocities generally match closely, larger differences are seen at the port. This difference is responsible for the slight differences in jet shape in the mold (Figure 4) discussed previously, and is due to the more diffusive nature of the coarser mesh used for LES-FLUENT.

B. Mold Flow

To show the mold flow pattern and further compare the different models, time-averaged velocity magnitude contours and streamlines are presented at the mold midplane in Figure 9. All models

predict a classic symmetrical “double-roll” flow pattern, with two upper counter-rotating recirculation regions, and two lower recirculation regions. Along the top surface, velocity from the narrow face to the SEN is very slow, owing to the deep nozzle submergence. This might cause meniscus freezing surface defects in a real caster, but the flow system is useful for model evaluation.

The velocity contours are similar between the transient models, but significant differences are seen with steady SKE RANS, which underpredicts the jet spread. The thinner and more focused jet gives higher velocity in both the upper and lower recirculation regions. In addition, the jet angle is too shallow, causing even more excessive surface flow. The upper eye is too centered in overly-rounded upper rolls, relative to the LES flow, where the eye is closer to the narrow face. The lower eye is too high, relative to the elongated low eye of LES. These inaccuracies of SKE RANS are likely due to the assumption of isotropic turbulence and underprediction of swirl in the nozzle bottom, compounded by the recirculating nature of the flow, and the lower Reynolds number in the mold, which are known to cause problems [23].

In the transient models, the jet region is dominated by small turbulence scales, so attains right-left symmetry after only ~ 1 -2 sec of time averaging. This contrasts with the lower rolls, which are still asymmetrical even after ~ 21 -31 secs time averaging, which suggests the dominance of large scale structures in these regions. The upper rolls structures are intermediate. This asymmetry reduces with more time averaging. The “filtered” URANS is similar to the LES models, but, exhibits even more asymmetries in the upper and lower rolls.

The surface velocity predicted by different models at the mold-mid plane between wide faces is compared in Figure 10(a). The 3 transient methods all predict similar trends, although values are different. The LES-CU-FLOW profile is slowest. The steady SKE model gives a different profile close to SEN where it predicts reverse flow towards the narrow face. Across the rest of the surface, the steady SKE model matches the other models. All of the surface velocities are very slow, (5-7 times smaller than a typical caster (~ 0.3) [1] which is a major cause of the differences between models.

The vertical velocity across the mold predicted by different models 35 mm below surface at mold midplane is compared in Figure 10(b). The transient models all matched closely. Due to the jet being thinner with a shallower angle, the steady SKE predicts much stronger recirculation in the upper zone, with velocity ~ 5 times faster up the narrow face and ~ 2 times faster down near the SEN than LES.

The vertical velocity along a vertical line 2mm from the narrow face wall at mold midplane is presented in Figure 11. The profile shape from all models is classic for a double-roll flow pattern [5-6]. This velocity profile also indicates the behavior of vertical wall stress along the narrow face. The positive and negative peaks match the beginning of the upper and lower recirculation zones respectively. The crossing from positive to negative velocity denotes the stagnation/impingement point (~ 110 mm below the top free surface in all models). The transient models agree closely, except for minor differences in URANS in the lower recirculation. Steady SKE predicts significantly higher extremes, giving higher positive values in the upper region and lower negative values in the lower region. This mismatch of steady SKE is consistent with the other velocity results, and indicates that care must be taken when using this model.

C. Turbulence Quantities

The turbulent kinetic energy (TKE), Reynolds normal stress components which comprise TKE, and Reynolds shear stress components are evaluated in the nozzle and mold, comparing the different models. Figure 12 compares TKE profiles along the nozzle port center- and 2-mm-offset- vertical lines for four different models. As expected, TKE is much higher in the outward flowing region than in the reverse flow region. TKE along the 2mm-offset line is higher than along the center-line.

The Steady SKE and URANS models greatly underpredict TKE along both lines. URANS does not perform any better than steady SKE in resolving turbulence in nozzle. The LES-FLUENT and LES-CU-FLOW models give similar trends but higher TKE is produced with LES-CU-FLOW owing to its better resolution. This produces the strongly-fluctuating nose in the mold that better matches the measurements. The TKE of LES-CUFLOW is presented at the mold-mid

planes in Figure 13. Turbulence originates in the nozzle bottom, where a V-shaped pattern is seen, and decreases in magnitude as the jets move further into the mold.

The TKE of the RANS models (k) has a high error, underpredicting turbulence by $\sim 100\%$ in Figure 12, which is much higher than the 3-15% mismatch with the velocity predictions exiting the nozzle (Figure 8). The “filtered” URANS model performs slightly better, but still underpredicts TKE by $\sim 40\%$. Similar problems of RANS models in predicting turbulence have been found in previous work in channels [23], square ducts [23] and in continuous casting molds [15]. This is due in large part to the RANS model assumption that turbulence is isotropic, ignoring its variations in different directions. The TKE in LES is based on its true definition as the sum of three resolved components:

$$\text{TKE} = 0.5(\overline{u'u'} + \overline{v'v'} + \overline{w'w'}) \quad (13)$$

where $\overline{u'u'}$, $\overline{v'v'}$ and $\overline{w'w'}$ are the Reynolds normal stresses. The LES models predict all six independent components of the Reynolds stresses including the 3 normal and also 3 shear components, which indicate interactions between in-plane velocity fluctuations.

The four most significant Reynolds stress components from the CU-FLOW LES model in the two mold midplanes are shown in Figure 14. The most significant turbulent fluctuations are in the y-z plane (side view) near the bottom of the nozzle. These $\overline{w'w'}$ and $\overline{v'v'}$ normal Reynolds stress components signify the alternating rotation direction of the swirling flow in the well of the nozzle. The $\overline{v'v'}$ out-of-plane fluctuation is the largest component in the front view. The $\overline{w'w'}$ vertical component is the largest and most obvious component near the front and back of the nozzle bottom walls in the side view. Their importance is explored in more detail in Section VII-D. The x-z plane components ($\overline{w'w'}$, $\overline{u'u'}$, and $\overline{u'w'}$) in the front view follow the up-down wobbling of jet at the port exit, which causes the stair-stepping phenomenon [8]. These horizontal ($\overline{u'u'}$) and vertical ($\overline{w'w'}$) show how this wobbling extends into the mold region, accompanied by the swirl, as evidenced by the $\overline{v'v'}$ variations. Further insight into the turbulent velocity fluctuations quantified by these Reynolds stresses is revealed from the POD analysis in Section VII-D.

VII. TRANSIENT RESULTS

Having shown the superior accuracy of LES methodology, the predictions from CU-FLOW and LES-FLUENT were applied to further investigate the transient flow phenomena. Specifically, the model predictions of transient flow behavior are evaluated together with measurements at individual locations, followed by spectral analysis to reveal the main turbulent frequencies, and a proper orthogonal decomposition (POD) analysis to reveal the fundamental flow structures.

A. Transient flow patterns

Instantaneous flow patterns from three different transient models at mold mid-plane are shown in Figure 15(a)-(c). These instantaneous snapshots of velocity magnitude were taken near the end of each simulation. Since the developed turbulent flow fields continuously evolve with time and fluctuate during this “pseudo-steady-state” period, there is no correspondence in time among the simulations. Each snapshot shows typical features of the flow patterns captured by each model. Due to the fine mesh, LES-CU-FLOW captures much smaller scales than LES-FLUENT. The flow field in URANS is a lot smoother due to a coarse mesh with a much larger spatial and temporal filter sizes. The instantaneous flow patterns are consistent with the mean flow field discussed previously. The maximum instantaneous velocity at the mold-mid plane is $\sim 10\%$ higher than the maximum mean velocity.

B. Transient velocity comparison

Model predictions with LES-FLUENT and measurements of time histories of horizontal velocity are compared at five different locations in the mold, (points 1-5 in Figure 16), in Figure 17. The measurements were extracted using an ultrasonic Doppler shift velocity profiler with ultrasonic beam pulses sent from behind the narrow face wall into the GaInSn liquid along the transducer axis. Due to divergence of the beam, the measurement represents an average over a cylindrical volume, with ~ 0.7 mm thickness in the beam direction, and diameter that increases with distance from the narrow face. Figure 16 shows the three beams (emitted from blue cylinders), their slightly diverging cylinders (red lines), and the averaging volumes (rectangles) for the points investigated here. The overall temporal resolution was ~ 0.2 sec, for the data acquisition rate used to obtain the data presented here. To make fair, realistic comparisons with the high-resolution

LES model predictions, spatial averaging over the same volumes and moving centered temporal averaging of 0.2 sec was also performed on the model velocity results.

Close to the SEN at point 1, Figure 17(a), the horizontal history predicted by LES greatly exceeds the inaccurate measured signal. The predicted velocity (~ 1.2 m/s) is consistent with the actual mass flow rate through the port. With spatial and temporal averaging included, the predicted time variations are very similar to the measured signal. This figure also includes part of the actual LES velocity history predicted at this point, with the model resolution of ~ 0.0002 s time step and 0.2-2mm grid spacing. This high-resolution prediction reveals the high-amplitude, high-frequency fluctuations expected close to the SEN, for the large Reynolds number ($Re=42,000$) in this region.

The individual effects of temporal and spatial averaging are investigated further at point 2, Figure 17(b). This point is near the narrow face above the mean jet impingement region, so has much smaller velocity fluctuations and significantly lower frequencies. Both temporal/spatial-averaging together, and temporal averaging alone bring the predictions closer to the measured history. Spatial averaging alone has only a minor effect.

Including temporal averaging smooths the predictions so that they match well with the measured velocity histories at other points (point 3, 4 and 5) as well. Points 3 and 4 have stronger turbulence and thus higher frequencies and fluctuations than at point 2, but are smaller than at point 1. Figure 17(e) shows that the signals obtained with a moving average to match the measurement introduce a time delay. Offsetting the moving average backwards in time by 0.1s (half of the averaging interval) produces a signal that matches a central average of the real signal. Overall, the predictions agree well with the measurements, so long as proper temporal averaging is applied according to the 0.2s temporal filtering of the measurement method. The higher resolution of the LES model enables it to better capture the real high frequency fluctuations of the turbulent flow in this system.

C. Spectral analysis

To further clarify the real frequencies in velocity fluctuations, Figure 18 presents a mean-squared amplitude (MSA) power spectrum, according to the formulation in [10]. This gives the

distribution of energy with frequency, for velocity magnitude fluctuations at points 6 and 7 (See Figure 16). The general trend of increasing turbulent energy at lower frequencies is consistent with previous work [5, 10]. As expected, point 6 which is close to the SEN shows much higher energy, mainly distributed from 3-100 Hz, relative to point 7, which is near the narrow face. This behavior of increasing velocity fluctuations at higher frequency is consistent with the higher Reynolds number. According to the power spectrum, frequencies above 5 Hz (0.2s period) are important. These higher frequencies represent small scale, medium to low energy turbulent eddies which cannot be captured by the measurements.

D. Proper orthogonal decomposition and flow variations in the nozzle bottom-well

Proper orthogonal decomposition (POD) has been applied to gain deeper insight into the fundamental transient flow structures that govern the fluctuations of the velocity field, according to the formulation in [45-46]. This technique separates the complicated spatial and temporal-dependent fluctuations of the real 3-D transient velocity field, $u'_z(\mathbf{x}, t)$, into a weighted sum of spatially-varying characteristic modal functions, by performing a single-value decomposition (SVD) [45-46],

$$u'_z(\mathbf{x}, t) = \sum_{k=1}^M a_k(t) \phi_k(\mathbf{x}) \quad (14)$$

where $\phi_k(\mathbf{x})$ are orthonormal basis functions which define a particular velocity variation field and $a_k(t)$ are the temporal coefficients. The first few terms provide a low-dimensional visually-insightful description of the real high-dimensional transient behavior. The representation naturally becomes more accurate by including more terms (larger M).

Writing the discrete data set, $u'_z(\mathbf{x}, t)$ in the form of a matrix $[U'_z]$, with t in rows and \mathbf{x} in columns, the SVD of $[U'_z]$ is

$$[U'_z] = [U][S][V]^T \quad (15)$$

where $[U]$ and $[V]$ are orthogonal matrices and $[S]$ is a diagonal matrix. Further defining $[W]$ as $[U][S]$ gives $[U'_z] = [W][V]^T$, where the k^{th} column of $[W]$ is $a_k(t)$ and the k^{th} row of $[V]^T$ is $\phi_k(x)$. The matrix $[S]$ has diagonal elements in decreasing order as $s_1 \geq s_2 \geq s_3 \geq s_4 \dots s_q \geq 0$, where $q = \min(M, N)$; s_i 's are called singular values and the square of each s value represents the velocity fluctuation energy in the corresponding orthogonal mode (k^{th} row of V^T). The k^{th} rank approximation of $[U'_z]$ is defined as Eq. (15) with $s_{k+1} = s_{k+2} \dots = s_q = 0$.

To perform SVD, the velocity fluctuation data was arranged in the following matrix form,

$$[U'_z] = \begin{bmatrix} \{u'_x\}_1 & \{u'_x\}_2 & \dots & \{u'_x\}_N & \{u'_y\}_1 & \{u'_y\}_2 & \dots & \{u'_y\}_N & \{u'_z\}_1 & \{u'_z\}_2 & \dots & \{u'_z\}_N \end{bmatrix} \quad (16)$$

where $\{u'_x\}_N$, $\{u'_y\}_N$ and $\{u'_z\}_N$ are column vectors representing a time series of three components of velocity at a particular point. Matrix $[U'_z]$ has size $M \times N$, where N is the number of spatial velocity-data points and M is the number of time instances.

In the current work, SVD was performed on the instantaneous velocity fluctuations predicted by LES-CU-FLOW at the mid-plane between the mold wide faces near the nozzle bottom and jet. This region was selected for POD analysis due to its strong transient behavior and large scale fluctuations of the wobbling jets exiting the two ports. Orthogonal modes were calculated by solving Eqs. 15-16 with a code in MATLAB. Matrix $[U'_z]$ was formulated for POD analysis based on 193 (x-) x 100(z-) spatial values for each velocity component selected for 6 sec with a time interval of 0.006s (total $N = 19300 \times 3 = 57900$, $M = 1000$).

Figure 19 presents contours of the most significant velocity variation components in the first four orthogonal modes, which contain $\sim 30\%$ of the fluctuation energy. In the first two modes (containing $\sim 22\%$ of the energy), the only significant component, v' , shows the alternating swirling flow in the well of the nozzle. In modes 3 and 4, the only significant components are the horizontal and vertical velocity variations (u' and w'), which are associated with up-down jet wobbling.

Figure 20 presents the temporal coefficients of these modes, and shows a positive/negative oscillatory behavior that indicates periodic switching of the direction of these modes. The singular values, which are a measure of the energy in each mode, are presented together with the cumulative energy fraction in Figure 21. The singular values reduce exponentially in their significance with increasing mode number. The first 400 modes contain ~88% of the total fluctuation energy.

The importance of different modes can be visualized by reconstructing instantaneous velocity profiles from their singular values. Four such reduced rank approximations of the fields are given in Figure 22. Figure 22(a) presents the time average of 6 sec data and 22(b) shows the original instantaneous velocity profile at $t=0$ sec. The rank-400 approximation, with 88% of the energy, approximates the original snapshot reasonably well. The rank-15 approximation, with 40% of energy, captures much of the nozzle velocity fluctuations, but misses most of the turbulent scales contained in the jet. This indicates that the turbulent flow in this mold is very complex, and contains important contributions from many different modes. This is likely a good thing for stabilizing the flow and avoiding quality problems.

The nozzle well swirl effects associated with the most-important 1st and 2nd modes can be understood better with the help of instantaneous velocities in the well of nozzle. Figure 23 presents instantaneous and time-average velocity vectors and contours at the mid-plane slice between narrow faces, looking into a nozzle port. As seen in Figure 23(c), the behavior of v in the 1st mode is due to swirl in the SEN bottom well, and has 15.66% of the total energy. The swirl direction of rotation periodically switches, which causes corresponding alternation of the v contours in Figure 19(a) and 23(c). This is also seen in the $\overline{v'v'}$ peaks in Figure 14(c). The alternating swirl also causes the strongest vertical flow to alternate between the front and back walls of the nozzle, as observed in the $\overline{w'w'}$ peaks in Figure 14(a) and in w in Figure 23(b). The temporal coefficient of the first mode in Figure 20 suggests that the switching frequency is ~3Hz. It is interesting to note that these continuously alternating rolls are not apparent in the symmetrical time average of this flow field, shown in Figure 23(d). A spectral analysis on v' in Figure 24 of a node in the nozzle bottom region further revealed the dominance of ~3-4Hz frequencies, which is consistent with the frequencies of the temporal coefficients of the 1st mode.

This revelation of swirl with periodic switching illustrates the power of the POD analysis, which matches and quantifies previous observations of the transient flow structures in the nozzle bottom well [3].

Another interesting mode is the up and down oscillation of the jet exiting the nozzle, which is manifested in u' and w' of mode 3, which is shown in Figure 19(c)-(d). The temporal coefficient of mode 3 in Figure 20 quantifies the period of this wobbling to be again ~ 3 -5Hz, which means it is likely related to the alternating swirl directions, as previously proposed [3]. This transient flow behavior has also been observed in previous work, where it was labeled “stair-step wobbling” [8]. To control mold turbulence, it seems important to control the 1st swirling mode, which sends turbulence to the mold in the form of u' and w' .

To identify further modes in other planes requires extension of the POD analysis to complete three dimensional instantaneous flow fields, which is beyond the scope of the current work. Even in two dimensions, however, this work shows the capability of POD analysis to illustrate and quantify transient structures in a new way, making it another powerful tool for the analysis of LES velocity results.

VIII. SUMMARY AND CONCLUSIONS

In this work, computational models are combined with measurements in a liquid GaInSn model to investigate turbulent flow in the nozzle and mold of a typical continuous casting process. This work also evaluates the performance of five different computational models, including two steady RANS models, “filtered” URANS, LES with FLUENT, and LES with an in-house GPU based CFD code (CU-FLOW).

LES predictions of time-averaged horizontal velocity match very well with the measurements, except where limitations in the measurements give unreasonably lower values close to the SEN and narrow face walls. Time and spatial averaging of the LES predictions to match the experimental resolution of < 5 Hz produces transient velocity histories that match closely with the measurements. Spectral analysis of the LES predictions confirms a large range of velocity fluctuation frequencies near the SEN (up to ~ 300 Hz, for 2 orders of magnitude drop in energy)

and close to narrow face (up to ~30Hz, for 2 orders of magnitude drop in energy. The fluctuation energy generally drops with distance from the nozzle, especially at the higher frequencies.

LES-CU-FLOW was the best model, with better accuracy than LES-FLUENT, owing to its higher resolution with a ~5 times finer mesh, and tremendously better computational efficiency, owing to its better numerics and use of a GPU methodology. The “filtered” URANS model performed in between LES and steady RANS, missing the high-frequency fluctuations, but capturing the long-time variations associated with large structures. The RANS models matched time-averaged velocity closely in the nozzle, but greatly underpredicted turbulence exiting the ports. This caused mismatches in the mold, especially with turbulence, so caution is needed when using steady RANS models. Among steady RANS models, SKE performed better than RKE.

The flow pattern is a stable, classic double-roll flow pattern, controlled by the strong turbulent nature of the flow structures in the bottom of the nozzle. The resolved Reynolds stresses and TKE show strong fluctuations in vertical velocity ($\overline{w'w'}$) and velocity normal to wide faces ($\overline{v'v'}$) associated with alternating directions of swirl in the bottom of the nozzle, and with wobbling of the jet in the mold. A POD analysis further reveals that the strongest transient flow structures are associated with nozzle bottom swirl and jet wobbling. The modes associated with this swirl contained 22% of the fluctuation energy. To control turbulence in the mold, it is important to control these modes.

ACKNOWLEDGMENTS

The authors are very grateful to K. Timmel and G. Gerbeth from MHD Department, Forschungszentrum Dresden-Rossendorf (FZD), Dresden, Germany for providing the velocity measurement data in GaInSn model. This work was supported by the Continuous Casting Consortium, Department of Mechanical Science & Engineering, University of Illinois at Urbana-Champaign, IL. ANSYS, Inc is acknowledged for providing FLUENT. Also, we would like to thank Silky Arora for helping us with data extraction codes for the POD analysis.

REFERENCES

- (1) B. G. Thomas, Fluid flow in the mold, Chapter 14 in Making, Shaping and Treating of Steel, 11th Edition, vol. 5, Casting Volume, Editor: A. Cramb, AISE Steel Foundation, Oct. 2003, Pittsburgh, PA, pp. 14.1-14.41.
- (2) B. G. Thomas, Modeling of continuous casting, Chapter 5 in Making, Shaping and Treating of Steel, 11th Edition, vol. 5, Casting Volume, Editor: A. Cramb, AISE Steel Foundation, Oct. 2003, Pittsburgh, PA, pp. 5.1-5.24.
- (3) D. E. Hershey, B. G. Thomas, and F. M. Najjar, Turbulent flow through bifurcated nozzles, Int. J. Num. Meth. in Fluids, 1993, 17(1), pp. 23-47.
- (4) B. G. Thomas, L. J. Mika and F. M. Najjar, Simulation of fluid flow inside a continuous slab-casting machine, Metall. Trans. B, 1990, vol. 21B, pp. 387-400.
- (5) R. Chaudhary, G.-G. Lee, B. G. Thomas, and S.-H. Kim, Transient Mold Fluid Flow with Well- and Mountain-Bottom Nozzles in Continuous Casting of Steel, Metall. Mat. Trans B, 2008, vol. 39B, no. 6, pp. 870-884.
- (6) R. Chaudhary, G.-G. Lee, B.G. Thomas, S.-M. Cho, S.-H. Kim, and O.-D. Kwon, Effect of Stopper-Rod Misalignment on Fluid Flow in Continuous Casting of Steel, Metall. Mat. Trans. B, 2011, vol. 42, 2, pp. 300-315.
- (7) X. Huang and B. G. Thomas, Modeling of transient flow phenomena in continuous casting of steel, Canadian Metallurgical Quarterly, 1998, vol. 37, no. 3-4, pp. 197-212.
- (8) Q. Yuan, S. Sivaramakrishnan, S.P. Vanka and B. G. Thomas, Computational and experimental study of turbulent flow in a 0.4 scale water model of a continuous steel caster, Metall. Mat. Trans. B, 2004, vol. 35B, pp. 967-982.
- (9) A. Ramos-Banderas, R. Sanchez-Perez, R. D. Morales, J. Palafox-Ramos, L. Demedices-Garcia, and M. Diaz-Cruz, Mathematical simulation and physical modeling of unsteady fluid flow in a water model of a slab mold, Metall. Mat. Trans. B, 2004, vol. 35B, pp. 449-460.

- (10) Q. Yuan, B. G. Thomas and S. P. Vanka, Study of transient flow and particle transport in continuous steel caster molds: Part I. Fluid flow, Metall Mat. Trans. B, 2004, vol. 35B, pp. 685-702.
- (11) B. Zhao, B. G. Thomas, S. P. Vanka and R. J. O'Malley, Transient fluid flow and superheat transport in continuous casting of steel slabs, Metall. Mat. Trans. B., 2005, vol. 36B, pp. 801-823.
- (12) Z.-D. Qian and Y.-L. Wu, Large eddy simulation of turbulent flow with the effects of DC magnetic field and vortex brake application in continuous casting, ISIJ International, 2004, vol. 44, no. 1, pp. 100-107.
- (13) R. Liu, W. Ji, J. Li, H. Shen, and B. Liu, Numerical simulation of transient flow patterns of upper rolls in continuous slab casting moulds, Steel Research Int., 2008, 79, no. 8, pp. 50-55.
- (14) K. Pericleous, G. Djambazov, J. F. Domgin and P. Gardin, Turbulence Model Performance in Continuous Casting Simulations, Proc. of the Sixth International Conf. on Engineering Computational Technology, Civil-Comp Press, Stirlingshire, UK, 2008.
- (15) B. G. Thomas, Q. Yuan, S. Sivaramakrishnan, T. Shi, S. P. Vanka and M. B. Assar, Comparison of four methods to evaluate fluid velocities in a continuous slab casting mold, ISIJ Int., 2001, vol. 41, no. 10, pp. 1262-1271.
- (16) Yuan, Q., B. Zhao, S.P. Vanka, and B.G. Thomas; "Study of Computational Issues in Simulation of Transient Flow in Continuous Casting", Steel Research International, Special Issue: Simulation of Fluid Flow in Metallurgy, Jan. 2005, Vol. 76, No. 1, pp. 33-43.
- (17) K. Timmel, S. Eckert, G. Gerbeth, F. Stefani, and T. Wondrak, Experimental modeling of the continuous casting process of steel using low melting point alloys – the LIMMCAST program, ISIJ International, 2010, 50, No. 8, pp. 1134-1141.
- (18) K. Timmel, S. Eckert, and G. Gerbeth, Experimental investigation of the flow in a continuous-casting mold under the influence of a transverse, direct current magnetic field, Metall. Mat. Trans. B, 2011, vol. 42, 1, pp. 68-80.

- (19) K. Timmel, X. Miao, S. Eckert, D. Lucas, and G. Gerbeth, Experimental and numerical modeling of the steel flow in a continuous casting mould under the influence of a transverse DC magnetic field, *Magnetohydrodynamics*, 2010, vol. 46, 4, pp. 337-448.
- (20) S. B. Pope, *Turbulent Flows*, 2000, Cambridge University Press, Cambridge, United Kindom.
- (21) J. O. Hinze, *Turbulence*, McGraw-Hill Publishing Company, 1975, New York.
- (22) B. E. Launder, and D. B. Spalding, *Mathematical Models of Turbulence*. 1972: London Academic Press.
- (23) R. Chaudhary, B.G. Thomas and S.P. Vanka, Evaluation of turbulence models in MHD channel and square duct flows, CCC 201011, Continuous Casting Consortium Report, Dept. of Mechanical Sc & Eng., University of Illinois at Urbana-Champaign, IL.
- (24) FLUENT6.3-Manual (2007), ANSYS Inc., 10 Cavendish Court, Lebanon, NH, USA.
- (25) B. Kader, Temperature and concentration profiles in fully turbulent boundary layers, *Int. J. Heat Mass Transfer*, 1981, 24(9), pp. 1541-1544.
- (26) M. Wolfstein, The velocity and temperature distribution of one-dimensional flow with turbulence augmentation and pressure gradient, *Int. J. Heat Mass transfer*, 1969, 12, pp. 301-318.
- (27) T.-H. Shih, W. W. Liou, A. Shabbir, Z. Yang, and J. Zhu, A New k - ϵ Eddy-Viscosity Model for High Reynolds Number Turbulent Flows - Model Development and Validation, *Computers & Fluids*, 1995, vol. 24(3), pp. 227-238.
- (28) S. T. Johansen, J. Wu, W. Shyy, Filter-based unsteady RANS computations, *Int. J. Heat and Fluid Flow*, 25, 2004, pp. 10-21.
- (29) R. Chaudhary, S.P. Vanka and B.G. Thomas, Direct numerical simulations of magnetic field effects on turbulent flow in a square duct, *Phys. of Fluids*, 22, 075102, 2010.

- (30) R. Chaudhary, A.F. Shinn, S. P. Vanka and B. G. Thomas, Direct Numerical Simulations of Transverse and Spanwise Magnetic Field Effects on Turbulent Flow in a 2:1 Aspect Ratio Rectangular Duct, *Computers & Fluids*, Submitted, Nov. 2010.
- (31) A. F. Shinn, S. P. Vanka, and W. W. Hwu, Direct numerical simulation of turbulent flow in a square duct using a graphics processing unit (GPU), AIAA-2010-5029, 40th AIAA Fluid Dynamics Conference, June 2010.
- (32) J. Smagorinsky, General circulation experiments with the primitive equations I. The basic experiment, *Month. Wea. Rev.*, 1963, 92, pp. 99-164.
- (33) M. Germano, U. piomelli, P. Moin, W. H. Cabot, Dynamic subgrid-scale eddy viscosity model, In summer Workshop, Center for Turbulence Research, 1996, Stanford, CA.
- (34) D. K. Lilly, A proposed modification of the Germano subgrid-scale closure model, *Phys. Fluids*, 1992, vol. 4, pp. 633-635.
- (35) S.-E. Kim, Large eddy simulation using unstructured meshes and dynamic subgrid-scale turbulence models, Technical Report AIAA-2004-2548, 34th Fluid Dynamic Conference and Exhibit, June 2004, AIAA.
- (36) W.-W. Kim and S. Menon, Application of the localized dynamic subgrid-scale model to turbulent wall-bounded flows, Technical Report AIAA-97-0210, 35th Aerospace Science Meeting, Jan. 1997, AIAA.
- (37) F. Nicoud and F. Ducros, Subgrid-scale stress modeling based on the square of the velocity gradient tensor, *Flow, Turbulence and Combustion*, 1999, vol. 63(3), pp. 183-200.
- (38) H. Werner and H. Wengle, Large-eddy simulation of turbulence flow over and around a cube in a plate channel, in 8th symposium on turbulent shear flows, 1991, Munich, Germany.
- (39) P. Moin and J. Kim, Numerical investigation of turbulent channel flow, *J. Fluid Mech.*, 118, 1982, pp. 341-377.

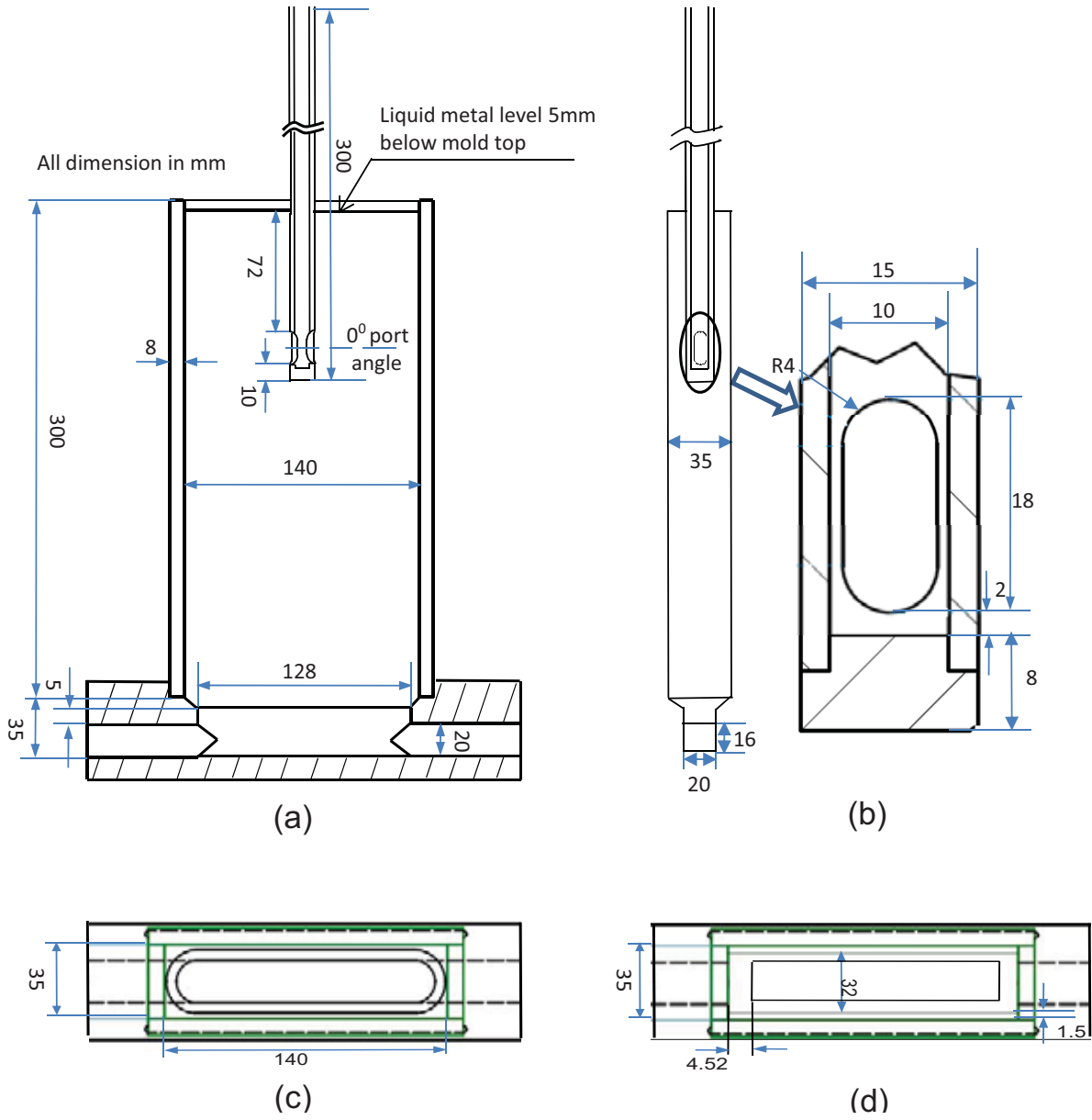
- (40) K. Y. M. Lai, M. Salcudean, S. Tanaka and R. I. L. Guthrie, Mathematical modeling of flows in large tundish systems in steelmaking, *Metall. Mat. Trans. B*, 17B, 1986, pp. 449-459.
- (41) M. H. Baba-Ahmadi and G. Tabor, Inlet conditions for LES using mapping and feedback control, *Computers & Fluids*, 38, 6, 2009, pp. 1299-1311.
- (42) A. Sohankar, C. Norberg, and L. Davidson, Low-Reynolds-number flow around a square cylinder at incidence: Study of blockage, onset of vortex shedding and outlet boundary condition, *Int. J. for Num. Meth. in Fluids*, 26, 1998, pp. 39-56.
- (43) M. Zagarola, and A. Smits, Mean-flow scaling of turbulent pipe flow, *J. Fluid Mech.*, 373, 1998, pp. 33-79.
- (44) H. Bai, and B.G. Thomas, Turbulent Flow of Liquid Steel and Argon Bubbles in Slide-gate Tundish Nozzles: Part I. Model Development and Validation, *Metall. Mat. Trans. B*, 2001, 32(2), pp. 253-267.
- (45) P. Holmes, J. L. Lumley, and G. Berkooz, *Turbulence, Coherent Structures, Dynamical Systems and Symmetry*, Cambridge University Press, UK, 1996.
- (46) A. Chatterjee, An introduction to proper orthogonal decomposition, *Current Science*, 78, 7, 10, April 2000, pp. 808-817.

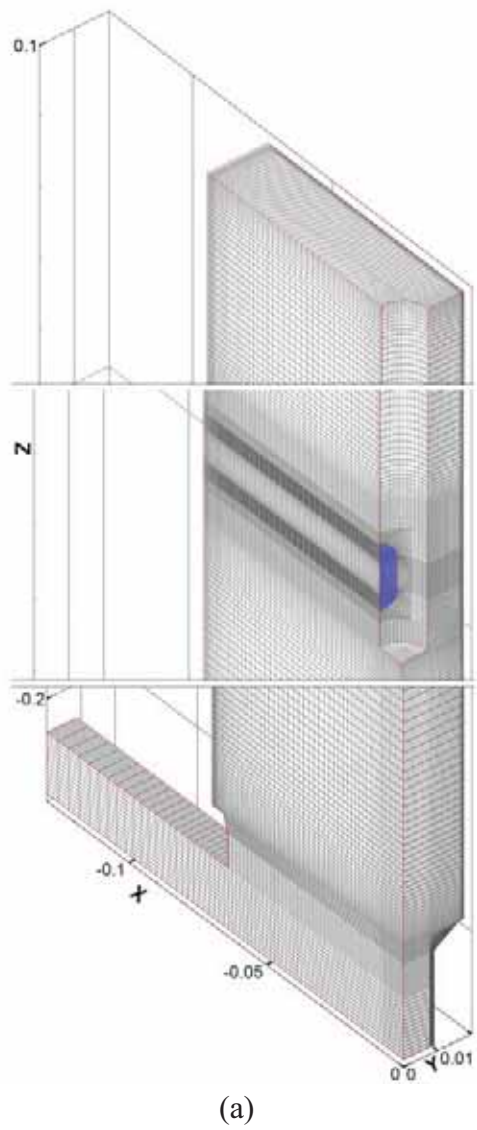
Table-1 Process parameters

Volume flow rate	110 ml/s
Nozzle inlet bulk velocity	1.4 m/s
Casting speed	1.35 m/min
Mold width	140 mm
Mold thickness	35 mm
Mold length	330 mm
Total nozzle height	300 mm
Nozzle port dimension	8mm(width)×18mm(height)
Nozzle bore diameter(inner/outer)	10mm/15mm
Nozzle port angle	0 degree
SEN submergence depth	72mm
Density(ρ)	6360 kg/m ³
Dynamic viscosity(μ)	0.00216 kg/m s

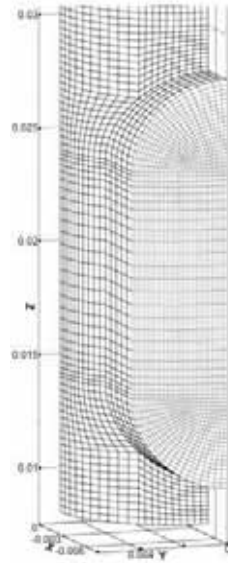
Table-2 Comparison of the jet characteristics in Steady SKE, filtered URANS and LES

Properties	Steady SKE model	Filtered URANS (SKE)	LES model (FLUENT)
	Left port	Left port	Left port
Weighted average nozzle port velocity in x-direction(outward)(m/s)	0.816	0.577	0.71
Weighted average nozzle port velocity in y-direction(horizontal)(m/s)	0.073	0.0932	0.108
Weighted average nozzle port velocity in z-direction(downward)(m/s)	0.52	0.543	0.565
Weighted average nozzle port turbulent kinetic energy (m ² /s ²)	0.084	0.0847	0.142
Weighted average nozzle port turbulent kinetic energy dissipation rate (m ² /s ³)	15.5	15.8	---
Vertical jet angle (degree)	32.5	43.3	38.5
Horizontal jet angle (degree)	0.0	0.0	0.0
Horizontal spread (half) angle (degree)	5.1	9.2	8.6
Average jet speed (m/s)	0.97	0.8	0.91
Back-flow zone (%)	34.0	17.6	25.1

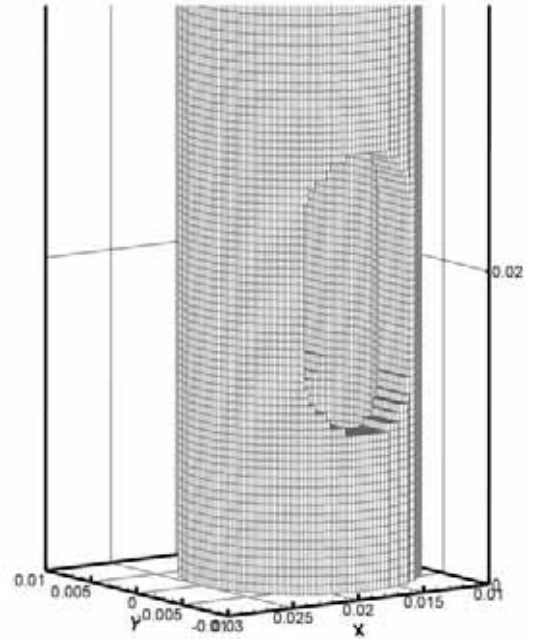




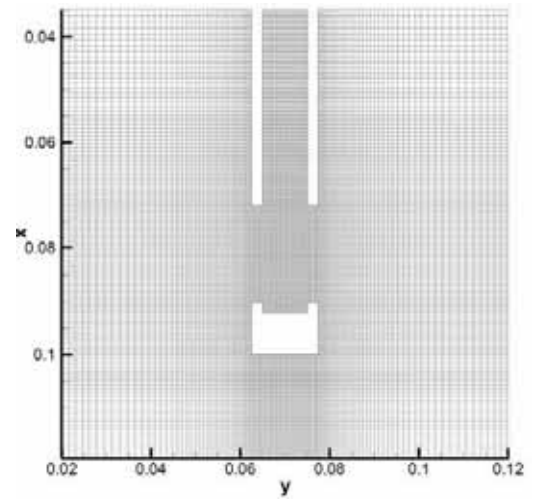
(a)



(b)



(c)



(d)

Fig-2 Computational meshes (a) Mold of steady RANS quarter-domain (~ 0.6 million cells) (b) Nozzle-port of steady RANS mesh (c) Nozzle mesh surfaces of LES-CU-FLOW (~ 7 million cells) (d) Mold mid-plane mesh of LES-CU-FLOW

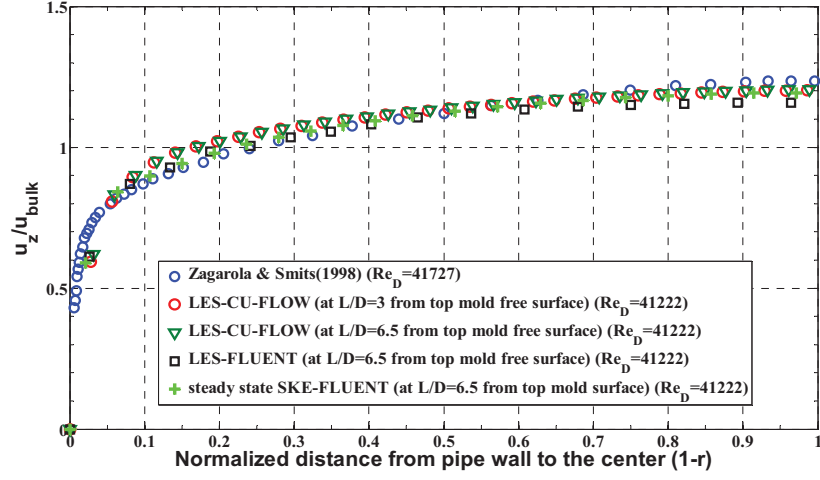


Fig-3 Axial velocity along nozzle radius (horizontal bisector) predicted by different models compared with measurements of Zagarola et al [43].

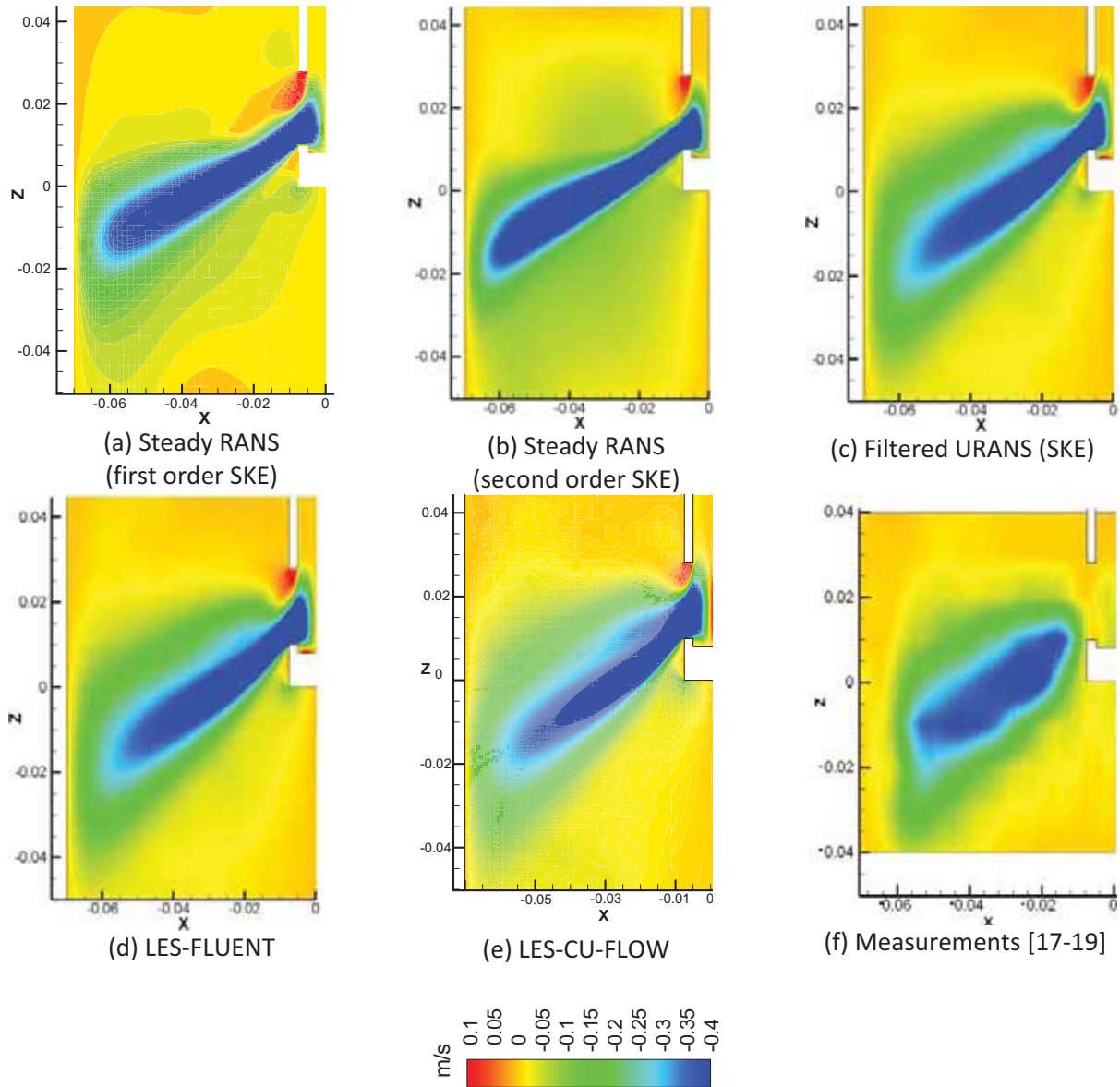
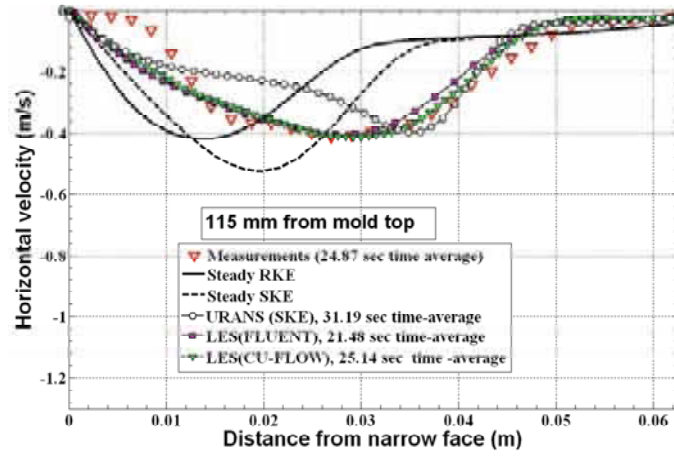
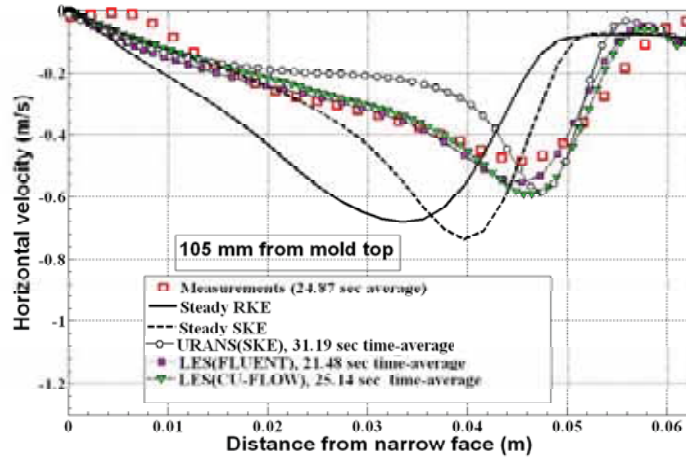


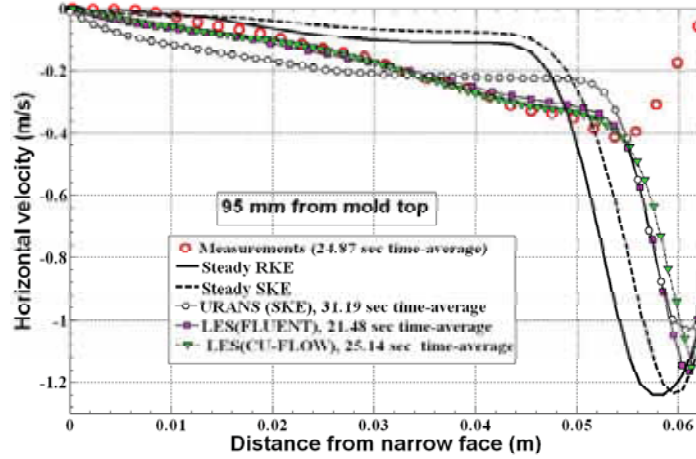
Fig-4 Average horizontal velocity contours in the mold mid-plane compared between different models and measurements.



(a) at 115 mm from mold top



(b) at 105 mm from mold top



(c) at 95 mm from mold top

Fig-5 Average horizontal velocity along three horizontal lines predicted by different models compared with measurements

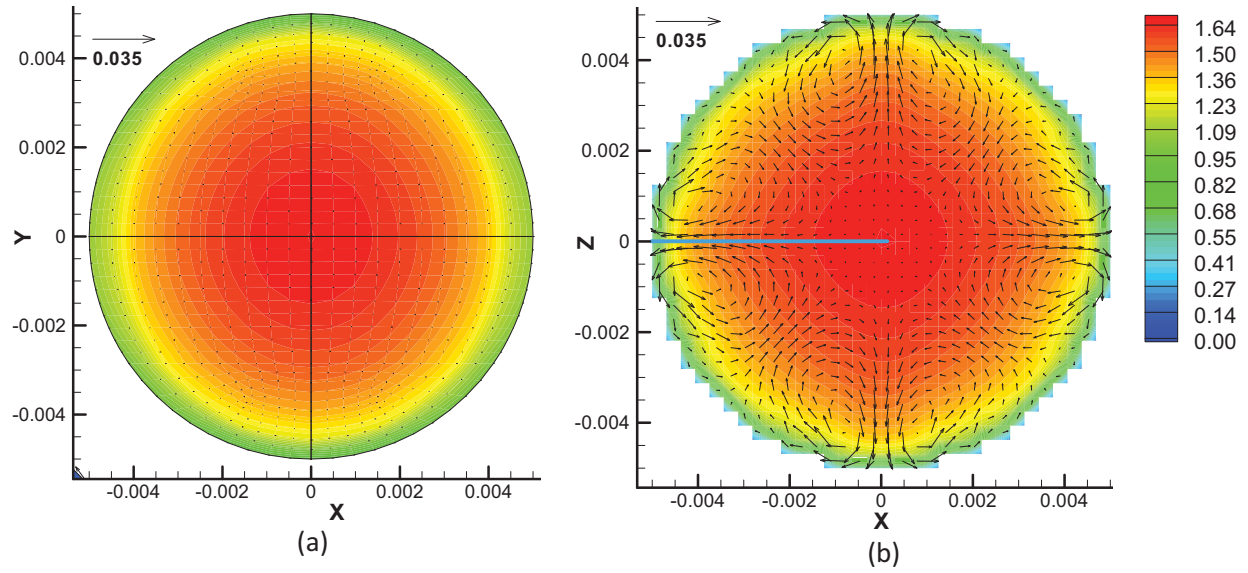


Fig-6 Axial velocity (m/s) with secondary velocity vectors at nozzle bore cross-section (a) steady SKE: ensemble-average (b) LES-CU-FLOW: time average

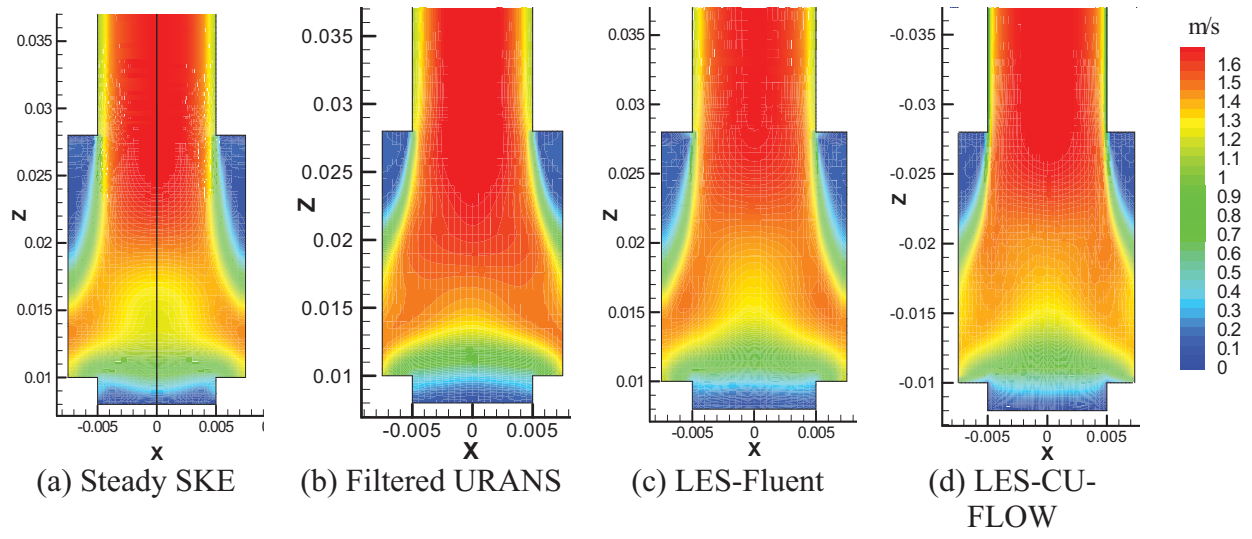


Fig-7 Average velocity magnitude contours in nozzle mid-plane near bottom comparing (a) Steady SKE (b) Filtered URANS (c) LES-FLUENT (d) LES-CU-FLOW

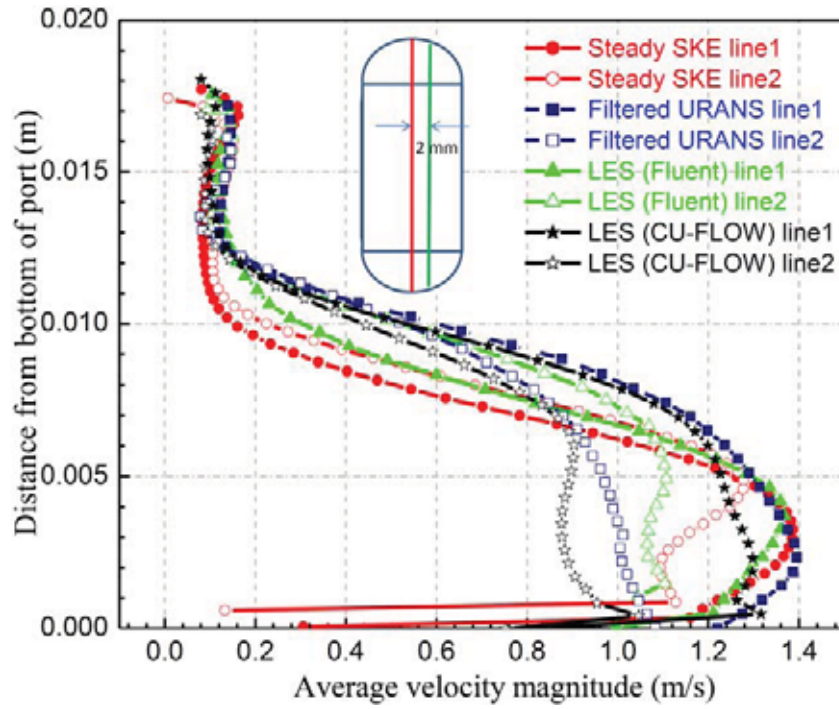


Fig-8 Comparison of port velocity magnitude along two vertical lines in outlet plane

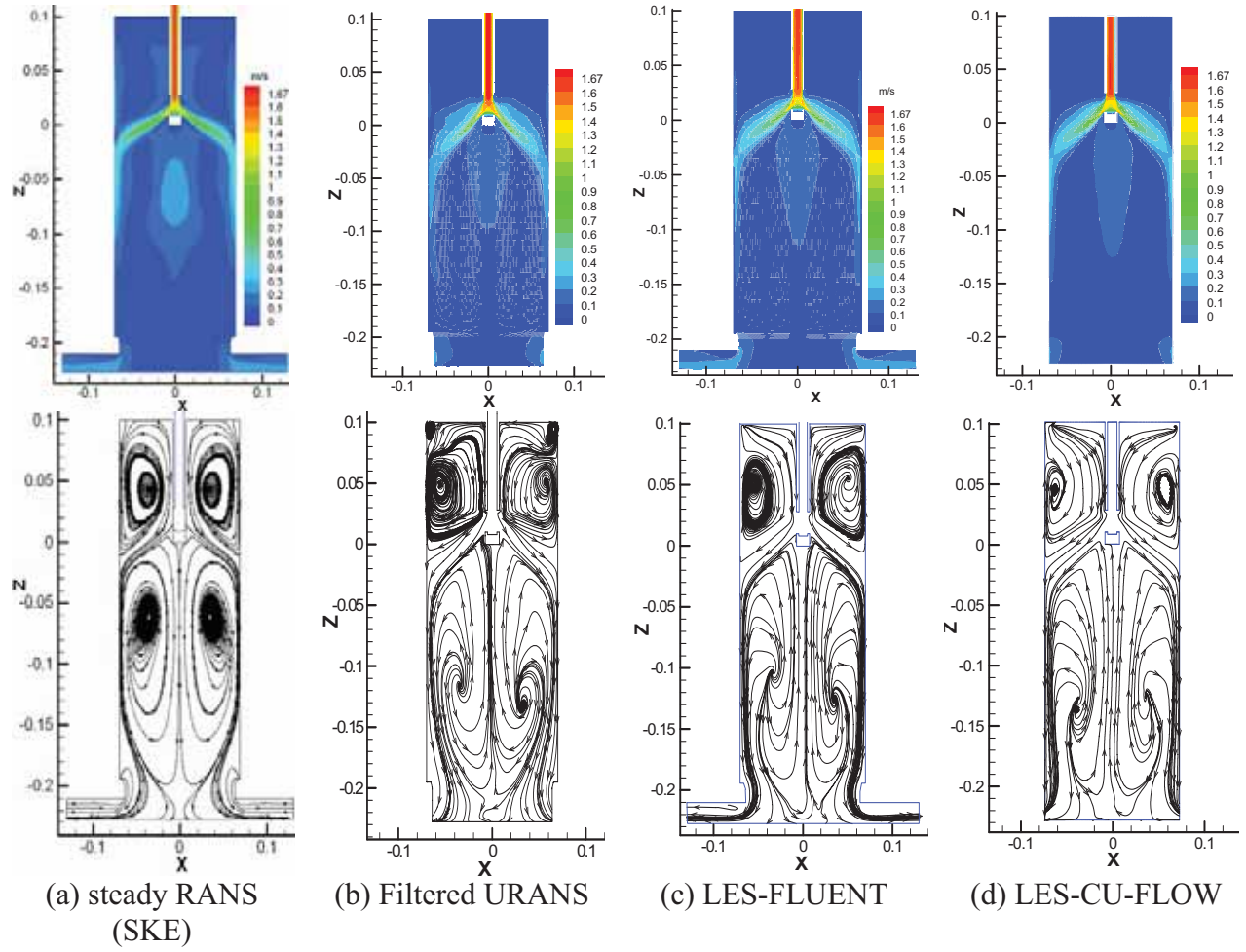


Fig-9 Comparison of time/ensemble average velocity magnitude(above) and streamline(below) at the mold mid-plane between wide faces

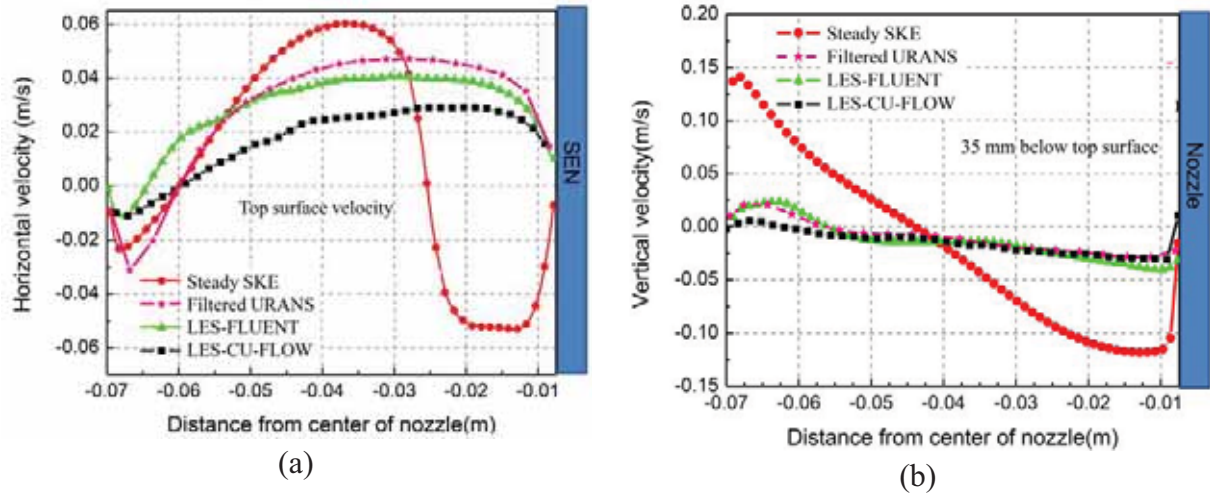


Fig-10 Average velocity profile at mold mid-plane comparing different models (a) horizontal velocity at top surface (b) vertical velocity at 35mm below top surface

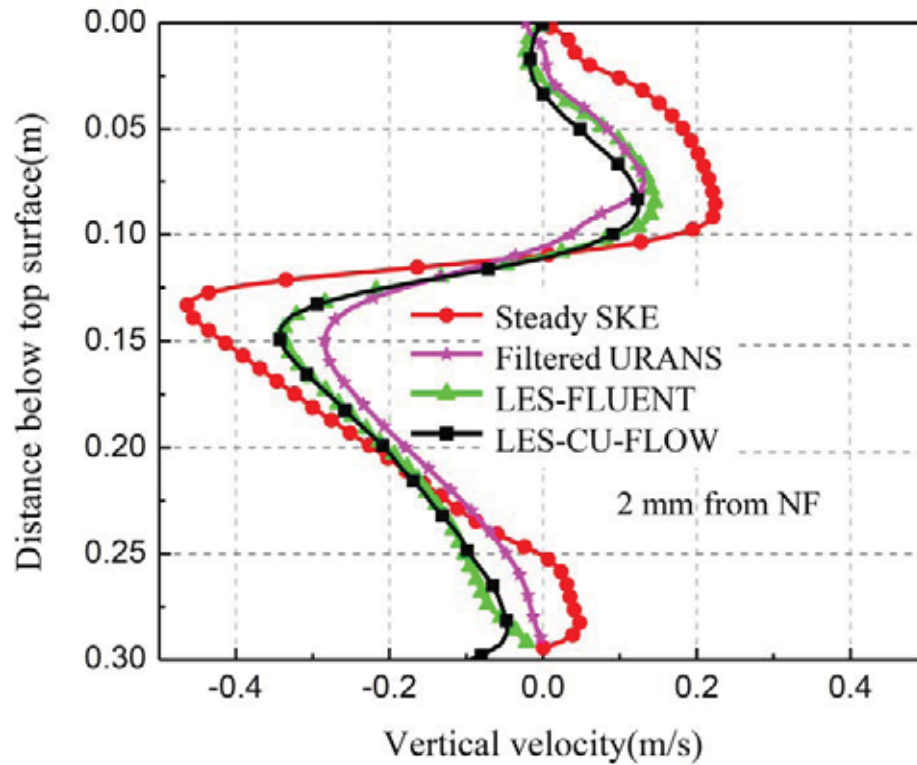


Fig-11 Comparison of time/ensemble average vertical velocity in different models at 2 mm from NF along mold length

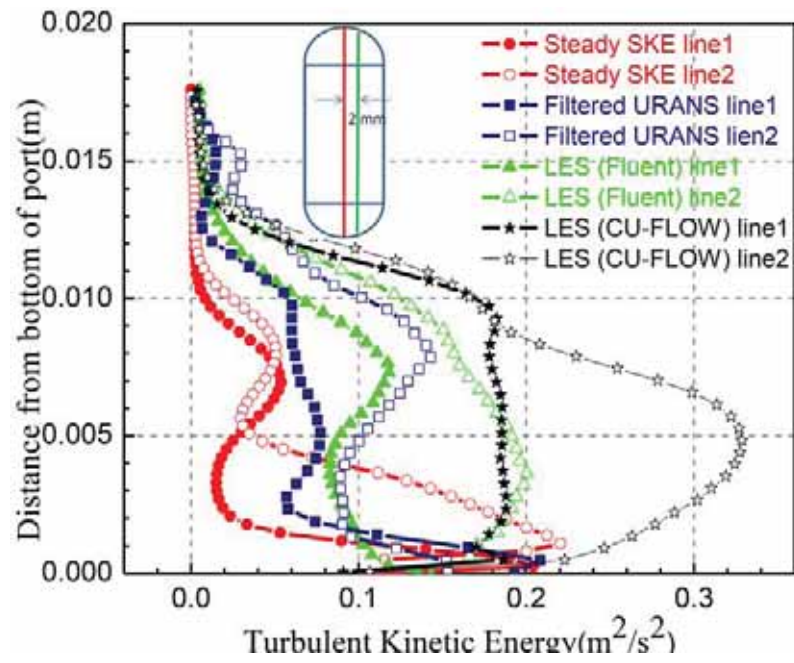


Fig-12 Comparison of TKE predicted by different models along two vertical lines at the port

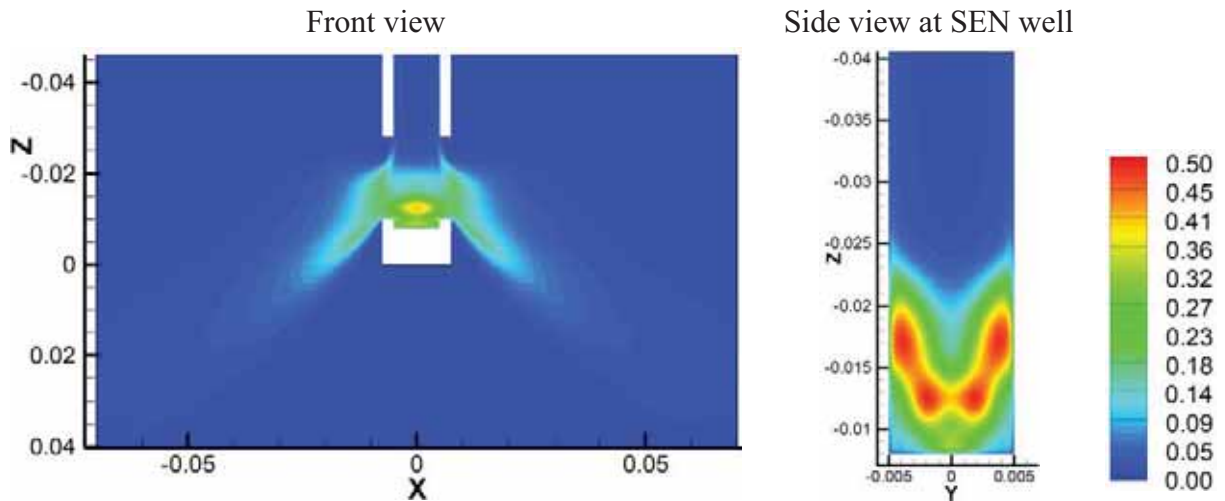


Fig-13 Resolved turbulent kinetic energy at mold mid-planes between wide and narrow faces

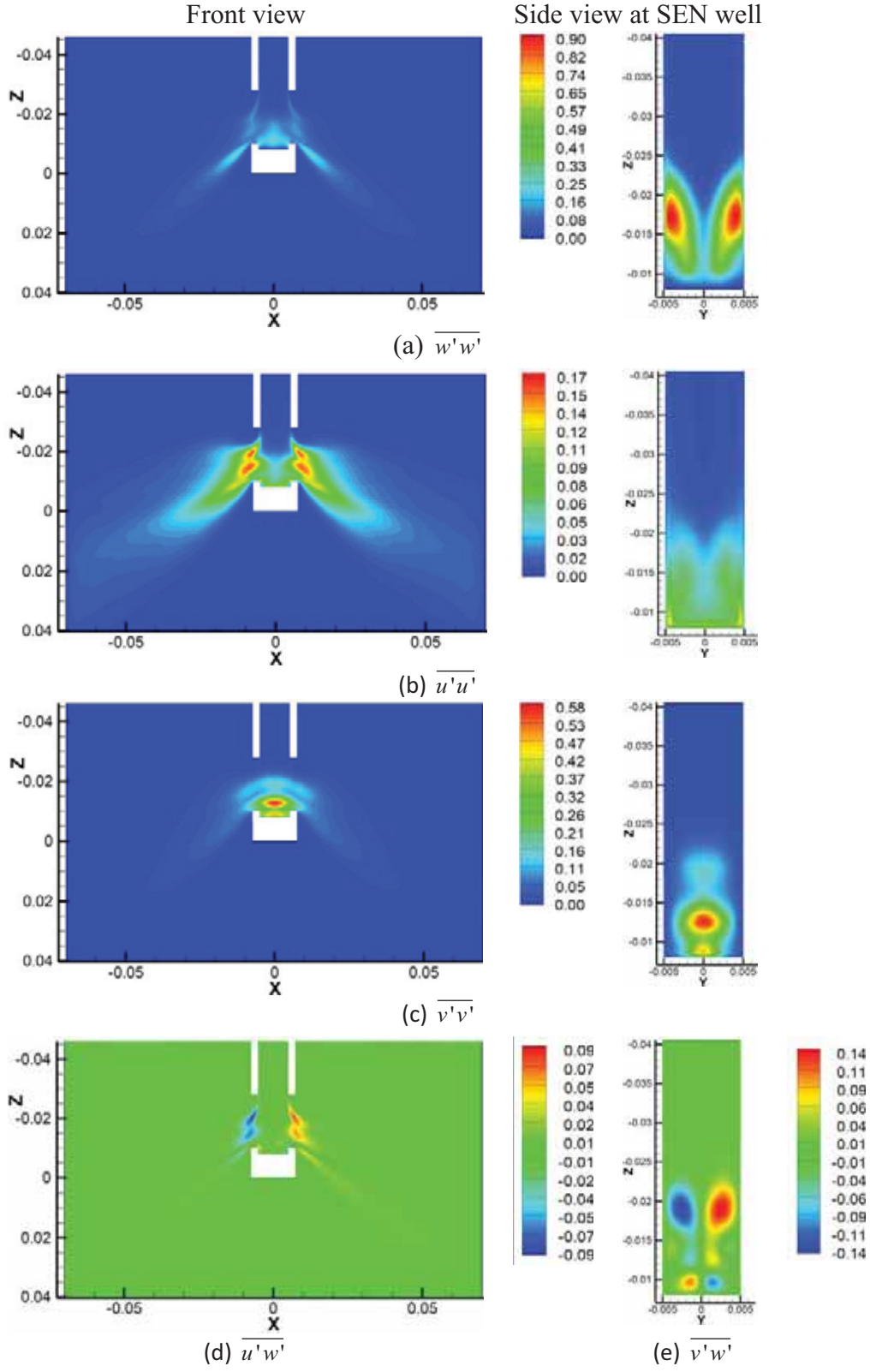


Fig-14 Resolved Reynolds normal and in-plane shear stresses at mold mid-planes between wide and narrow faces

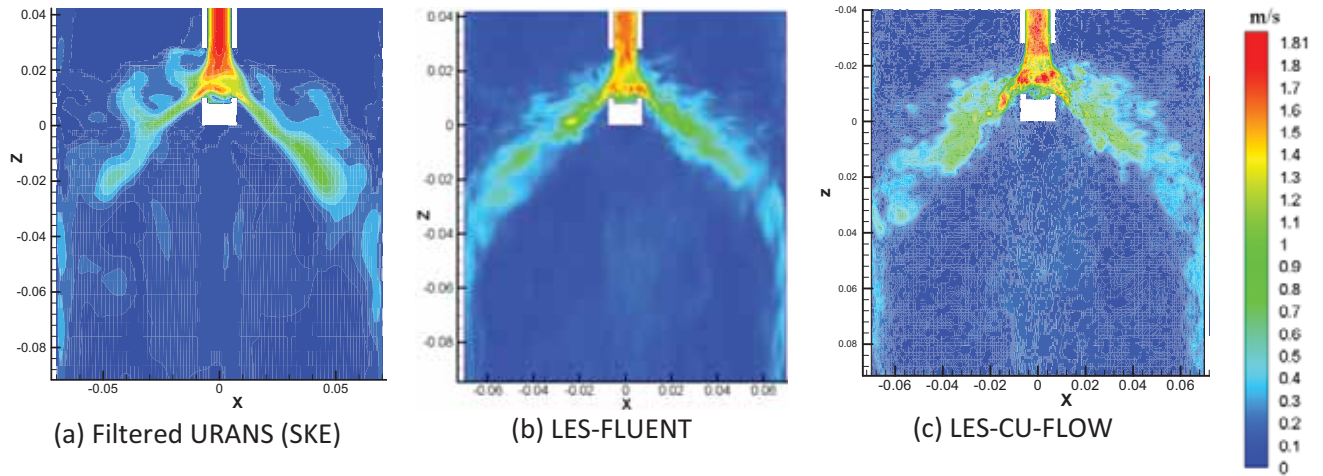


Fig-15 Instantaneous velocity magnitude contours comparing different transient models

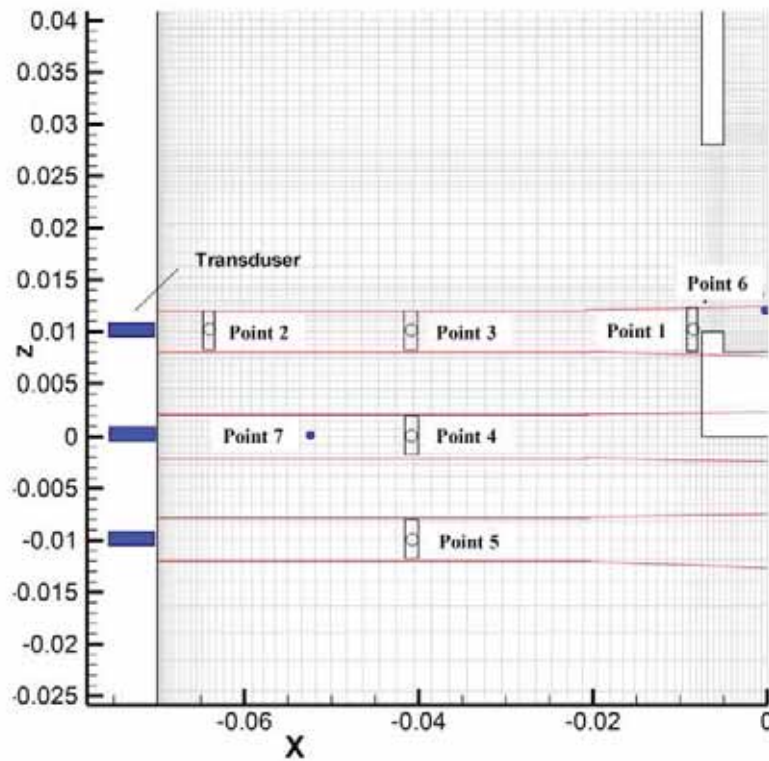


Fig-16 Spatial-averaging regions where instantaneous horizontal velocity points are evaluated in the midplane between widefaces. (Lines are boundaries of the cylindrical UDV measurement regions; coordinates in m)

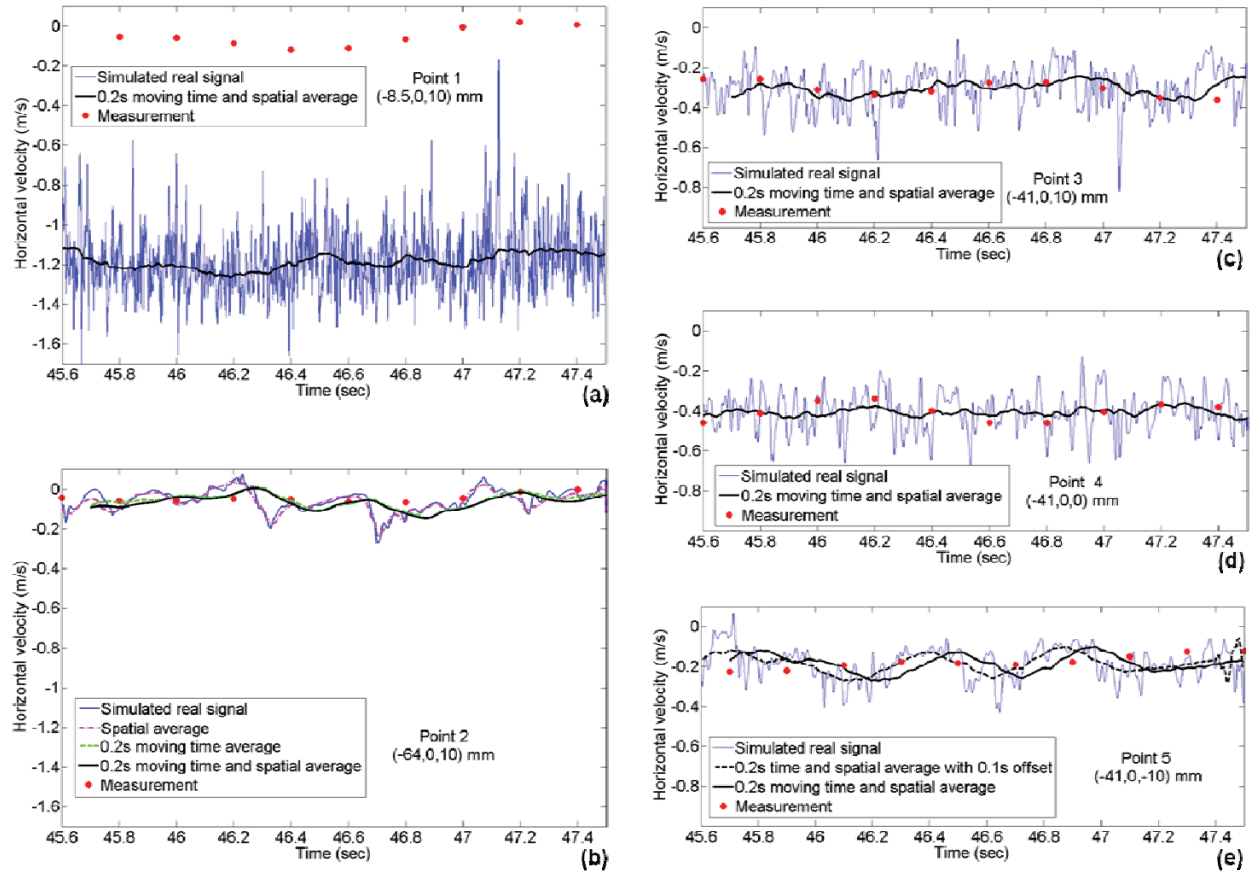


Fig-17 Instantaneous horizontal velocity histories comparing LES-FLUENT and measurements at various points (see Fig-16) in the nozzle and mold mid-plane (point coordinates in mm)

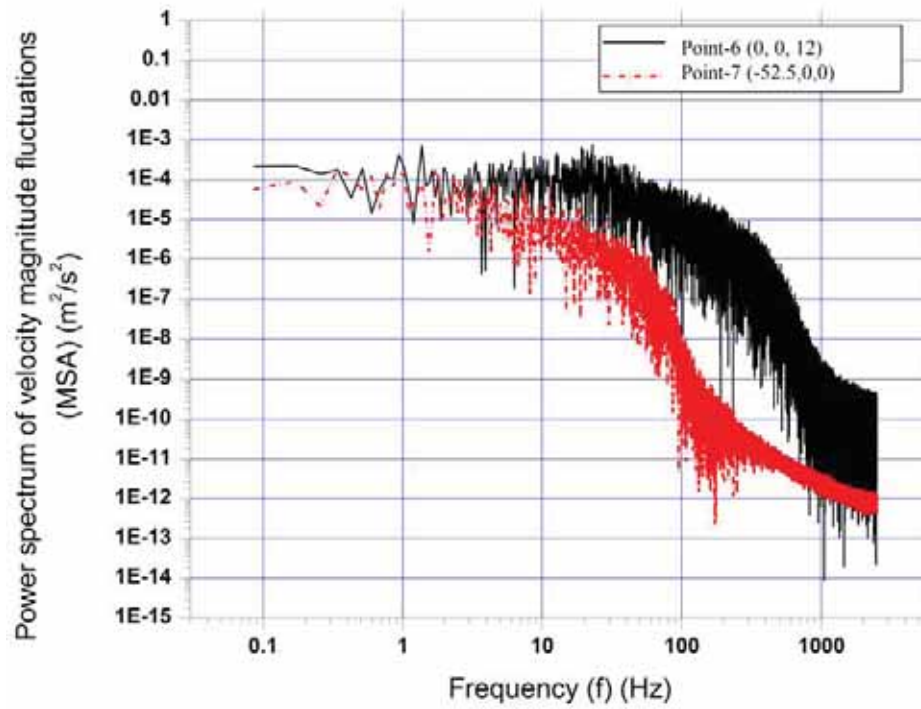


Fig-18 Power spectrum (Mean-Squared Amplitude) of instantaneous velocity magnitude fluctuations at two points (see Fig. 16) in the nozzle and mold

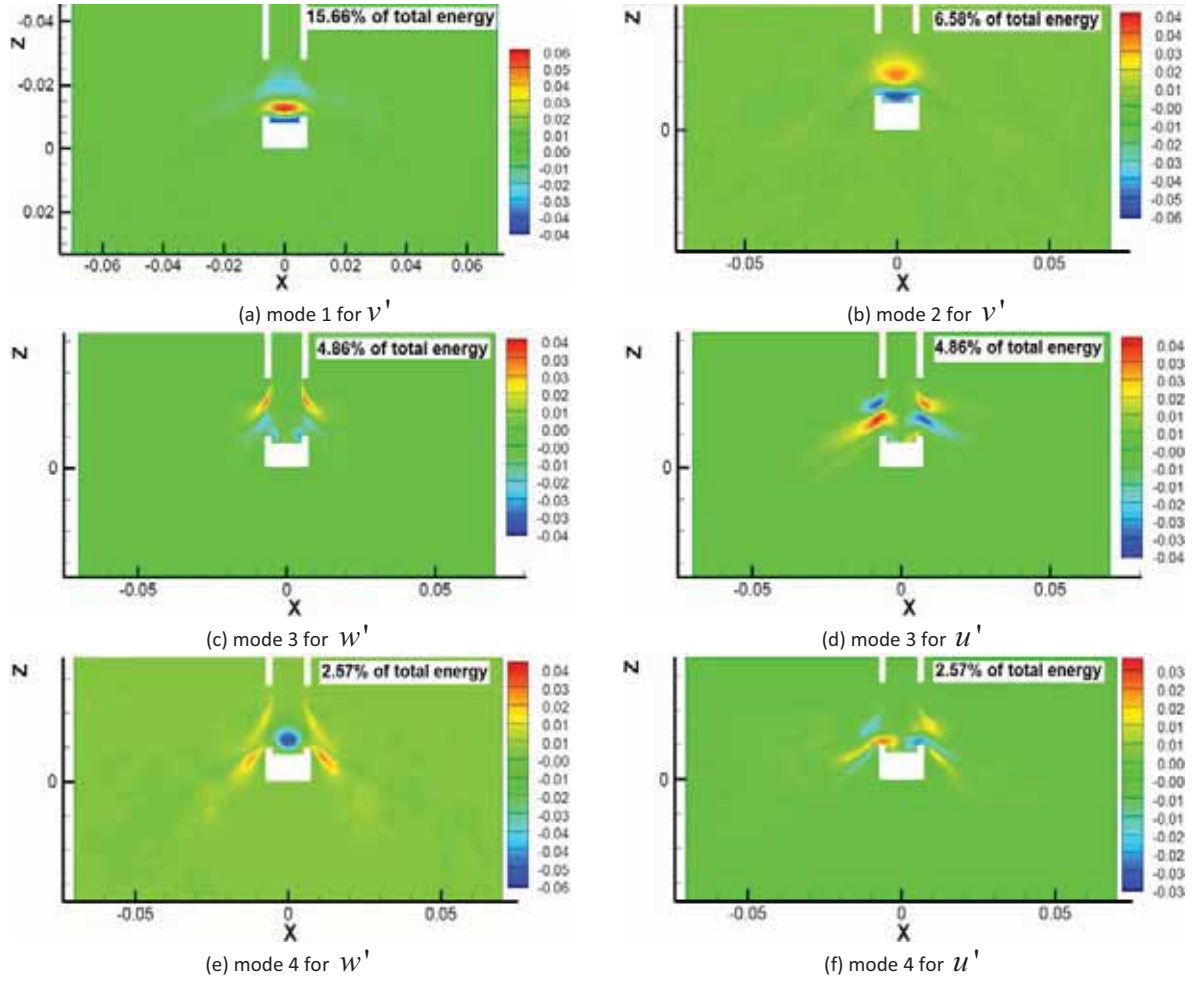


Fig-19 First four proper orthogonal decomposition (POD) modes (containing ~30% of total energy) showing different velocity component fluctuations (u' , v' , or w')

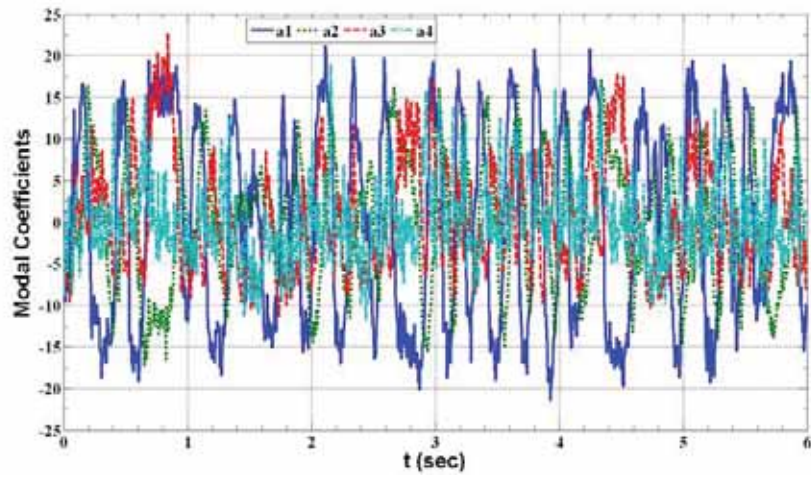


Fig-20 POD Modal coefficients (or Modal contributions)

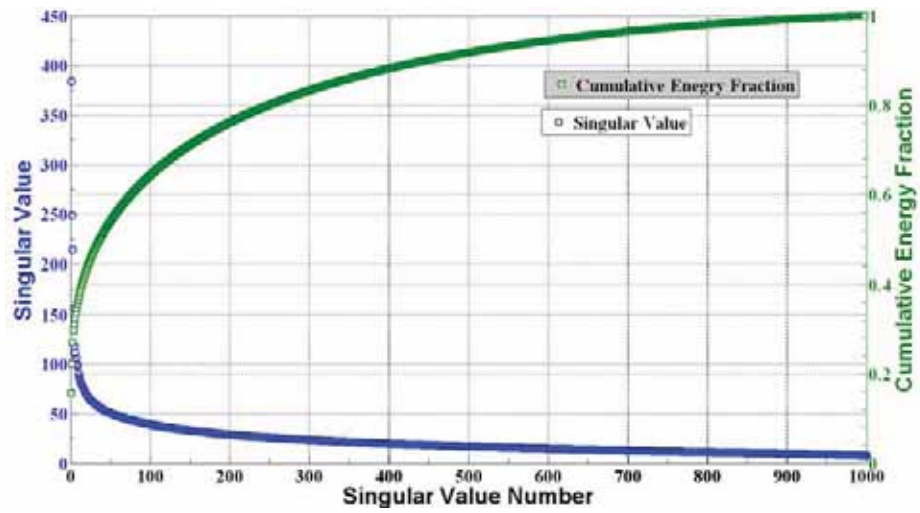


Fig-21 Singular values and cumulative energy in different POD modes of velocity fluctuations (\vec{u}')

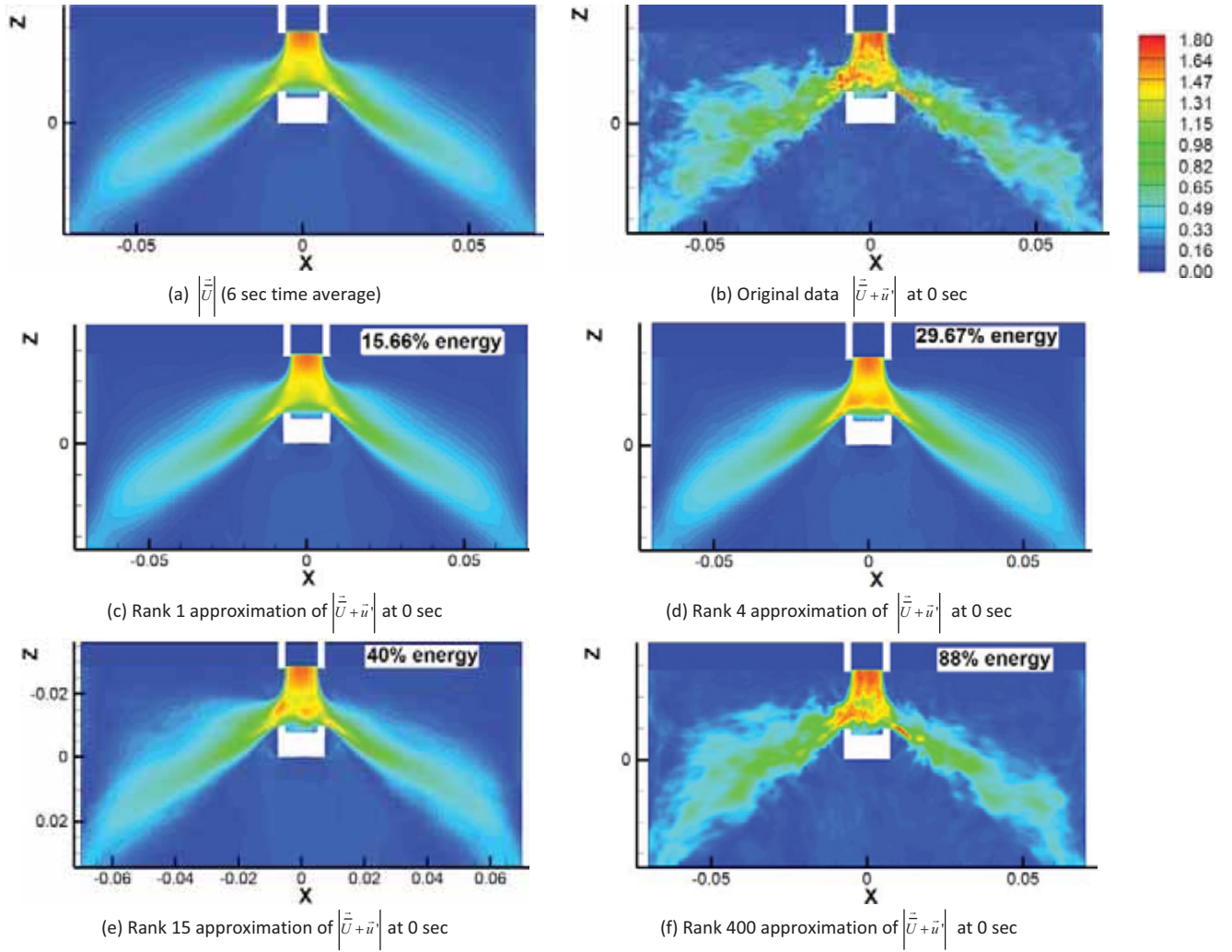


Fig-22 POD reconstructions of velocity magnitude in mold centerline showing contours of (a)Time-average and (b) an instantaneous snapshot calculated by LES CU-FLOW at 0s compared with (c-f) four approximations of the same snapshot using different ranks

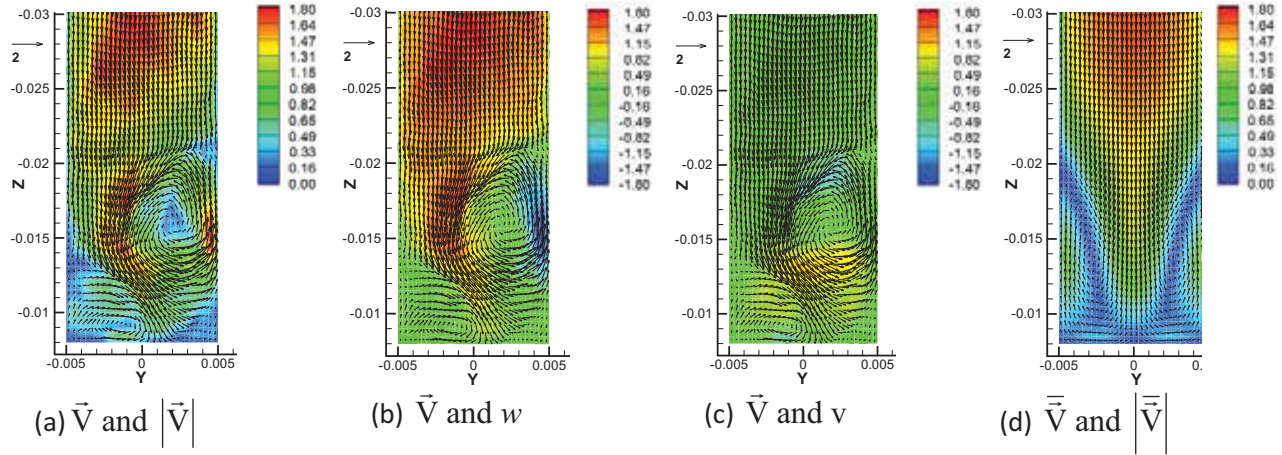


Fig-23 Flow pattern in the SEN bottom well midplane, showing an instantaneous velocity vector snapshot colored with contours of (a) velocity magnitude (b) vertical velocity and (c) horizontal velocity (d) Time-average velocity vectors and velocity magnitude contours

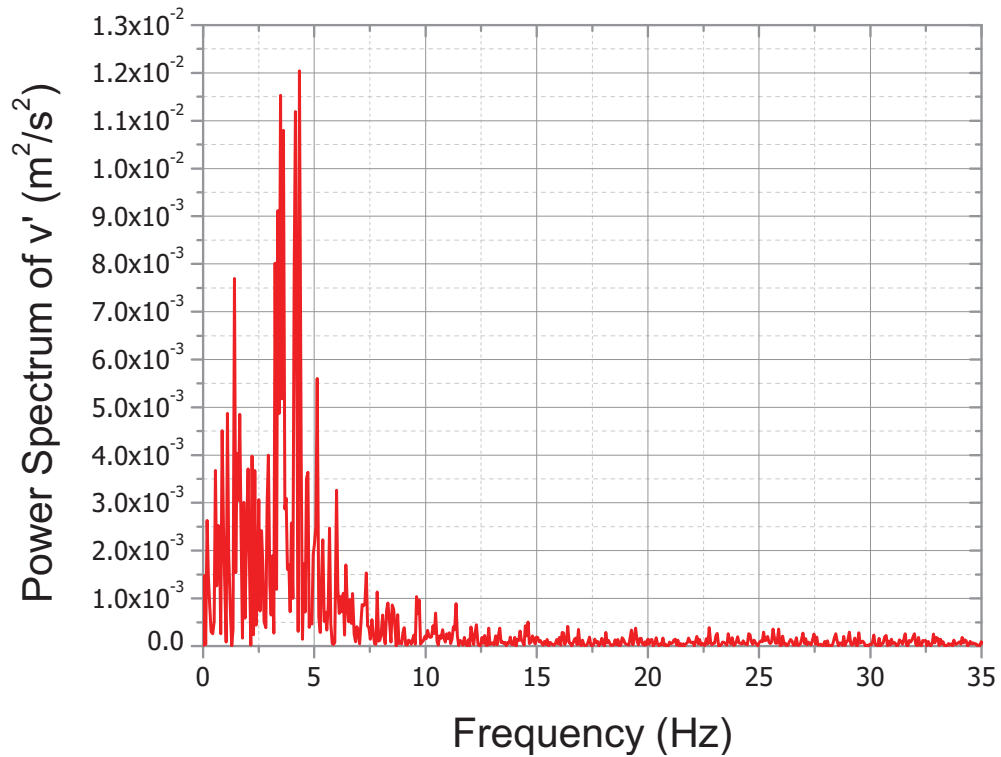


Fig-24 Power spectrum (MSA) of wide face normal velocity fluctuations at SEN nozzle bottom center at 95 mm below mold top